Redefining electrolyte efficiency: bridging the gap with a systematic samarium–copper co-doping approach for optimized conductivity in advanced semiconductor ionic fuel cell

Muhammad Shahid Sharif[1]**, Zuhra Tayyab**[2]**, Sajid Rauf**[2,*] ⓘ**, Muhammad Ahsan Masood**[1]**, MAK Yousaf Shah**[2]**, Muhammad Tayyab**[3]**, Abdullah N Alodhayb**[4] **and Bin Zhu**[1,*]

[1] School of Energy and Environment, Southeast University, Nanjing, People's Republic of China
[2] College of Mechatronics and Control Engineering, Shenzhen University, Shenzhen, Guangdong, People's Republic of China
[3] College of Materials Science and Engineering, Shenzhen University, Shenzhen, Guangdong, People's Republic of China
[4] Department of Physics and Astronomy, College of Science, King Saud University, Riyadh 11451, Saudi Arabia

E-mail: sajidrauf@szu.edu.cn and zhu-bin@seu.edu.cn

CrossMark

Abstract

Significant efforts have been dedicated to developing next-generation optimal electrolytes for high-performance low-temperature solid oxide fuel cells (SOFCs). In this study, we present an innovative co-doping strategy, incorporating samarium (Sm^{3+}) and copper (Cu^{2+}) into ceria ($Cu_xSm_{0.2-x}Ce_{0.8}O_2$, $x = 0$, 0.05, 0.10, 0.15). By leveraging Sm^{3+} and Cu^{2+} to create oxygen vacancies and Cu^{2+} to further induce the controlled electronic characteristics, we engineered a material with enhanced proton conductivity and efficient electronic transfer and ionic transport. Distribution of relaxation times and electrochemical impedance spectroscopy analyses revealed significantly reduced grain boundary resistance and efficient proton conduction over the temperature range of 320 °C to 520 °C. Notably, the optimized $Cu_{0.1}Sm_{0.1}Ce_{0.8}O_2$ composition achieved a peak power density of 902 mW cm^{-2} with appreciable ionic conductivity of 0.16 S cm^{-1} at 520 °C, demonstrating its potential as a high-performance electrolyte. UV-Vis analysis indicated a reduced band gap, while DC polarization measurements indicated electronic conductivity of 0.019 S cm^{-1}, suggesting the material possesses semiconducting properties suitable for the electrochemical applications. Advanced physical characterizations and their analysis provided detailed information of the materials, which are suitable for the fuel cell applications. In addition, the post stability of fuel cell device's characterizations provided the detail information and evident the stable behavior of the as-prepared optimal

---

* Authors to whom any correspondence should be addressed.

$Cu_{0.1}Sm_{0.1}Ce_{0.8}O_2$ (10-CSC) material acted as electrolyte. These findings position $Cu_{0.1}Sm_{0.1}Ce_{0.8}O_2$ as a promising candidate for intermediate-temperature SOFCs, representing a significant advancement in semiconductor ionic electrolyte materials.

Supplementary material for this article is available online

Keywords: samarium–copper co-doped ceria (CSC), oxygen vacancy engineering, optimized ionic–electronic conductivity (OIEC), protonic conductivity, low-temperature semiconductor ionic membrane fuel cells (LT-SIMFCs)

1. Introduction

As global energy demands surge and environmental concerns escalate, the quest for efficient, sustainable, and scalable energy solutions has never been more pressing. Among the diverse technologies under exploration, semiconductor ionic membrane fuel cells (SIMFCs) stand at the frontier of innovation, offering a promising route to clean energy generation [1, 2]. SIMFCs capitalize on the hybrid properties of semiconductor materials, bridging the gap between electronic and ionic conductors. This unique combination offers a pathway to overcoming many challenges associated with high-temperature fuel cells, particularly those linked to performance losses and material degradation at intermediate temperatures. A critical aspect of SIMFC performance is developing advanced electrolyte materials that can efficiently transport ions while minimizing electronic leakage [3, 4]. One material that has drawn significant attention in the context of intermediate-temperature fuel cell operation is ceria (CeO_2), valued for its excellent oxygen-ion conductivity and relatively low operating temperatures compared to conventional SOFC electrolytes [5, 6]. Doping strategies have been employed using numerous single dopants, like samarium and gadolinium, to enhance ionic conductivity in ceria by stabilizing oxygen vacancies to modify ceria's defect chemistry, enhancing oxygen vacancy formation and ionic conductivity, as reported in the literature [7]. Gadolinium-doped ceria (GDC) and samarium-doped ceria (SDC) materials have been employed as electrolyte membranes for intermediate-temperature SOFCs, where, SDC showed particularly high ionic conductivity due to efficient vacancy formation [7, 8]. These dopants operate by substituting Ce^{4+} with Sm^{3+} or Gd^{3+}, which introduces a charge imbalance that is compensated by the formation of oxygen vacancies, critical for oxygen-ion transport [9, 10]. Recent studies on doped ceria systems have revealed that incorporating transition metals like copper has the potential to enhance ionic conductivity as well as span operational temperature by improved electro-catalytic properties and generation of oxygen vacancies [11, 12]. While traditional doping with elements like Gd^{3+} or Sm^{3+} has been associated with certain limitations, using copper-like metals as co-dopants can potentially optimize both ionic and electronic transport properties. Hence, carefully selecting dopants with complementary roles, where co-doping allows researchers to tune the defect chemistry of the material finely, optimizing oxygen vacancy formation while utilizing electronic characteristics as a supporting property in materials acting as electrolytes [12, 13].

Samarium has a well-documented ability to stabilize oxygen vacancies [14], facilitated by the excellent electro-catalytic activity of copper, thereby promoting ionic conduction. The +3 state of samarium and the +2 state of copper interact with the +4 state of cerium, forming a defect structure that can improve the electrical properties of the proposed material's overall performance [12, 15, 16]. The presence of adjacent oxidation states (Sm^{+3}, Cu^{+2}, Ce^{+4}) may facilitate electron hopping, improving charge transport within the material. The interplay between these oxidation states may also facilitate the movement of electrons between adjacent species, which is expected to influence the band structure of the material, improving the electron-ion (E-I) coupling mechanism within the material. However, controlled electron transport is crucial, as excessive electronic conduction would undermine the electrolyte's effectiveness [11]. Alterations in the band gap could also result in more favorable conditions for charge transport, particularly the SIMFCs operate at the intermediate temperatures [4, 17].

Therefore, considering previous studies and their mechanisms, here we introduced a new strategy and mechanism by introduction of samarium and copper (5%, 10% and 15%) into CeO_2 ($Cu_xSm_{0.2-x}Ce_{0.8}O_2$, $x = 0$, 0.05, 0.10, 0.15), which leads to change in grain size and grain boundary properties, where both play a critical role in modulating the ionic conductivity [18]. Unlike conventional single-dopant or co-doping strategies, the co-doping of Sm^{3+} and Cu^{2+} introduces a synergistic effect, where Sm^{3+} contributes to stabilized oxygen vacancy formation and Cu^{2+} facilitates redox-active electronic transfer pathways while enhancing oxygen vacancy formation. This innovative approach leverages complementary dopant functionalities to achieve optimized mixed conduction pathways. The interplay between defect chemistry and microstructure due to Cu and Sm doping is a key factor in the performance of co-doped ceria electrolytes, where this study is primarily focused in this investigation. This study further aims to systematically investigate the impact of Sm-Cu co-doping on the electrochemical performance, semiconducting properties, and microstructure of ceria-based materials. The optimized ratio of Cu to Sm, we aim to develop a new class of electrolytes that can operate efficiently at lower operational temperatures, with minimal voltage loss and improved ionic conductivity. Furthermore, we systematically investigate how

varying concentrations of Sm and Cu influence both the microstructural and electrochemical properties of CeO_2. Our goal is to delicately balance the electronic conduction pathways introduced by high content of Cu doping while maximizing ionic conductivity through enhanced oxygen vacancy formation and morphological control.

2. Experimental materials

2.1. Materials availability and their implementation in synthesis of the proposed materials

The materials used in this study were of high purity and sourced from Sigma-Aldrich. Cerium (III) nitrate nonahydrate (ACS 99% purity), samarium (III) nitrate hexahydrate, copper nitrate hexahydrate (ACS 99%), and Sodium carbonate monohydrate (ACS 99%) were employed as the primary chemical precursors. Commercially available SDC was used. A co-precipitation method was applied to synthesize the $Cu_{0.1}Sm_{0.1}Ce_{0.8}O_2$ solid solution, where molar ratios for the cerium nitrate, samarium nitrate, and copper nitrate precursors were calculated according to the stoichiometric ratio and dissolved in deionized water (DI) under continuous stirring. The cerium nitrate solution was prepared in 300 ml of DI water and stirred at 400 rpm at the heating temperature of 60 °C. Simultaneously, copper nitrate and samarium nitrate solutions were prepared in distinct beakers in 100 ml of DI water. Afterward, the solutions of copper nitrate and samarium nitrate were poured into the cerium nitrate solution and stirred at 700 rpm for 3 h at 80 °C until complete dissolution. In addition, a concentration of 1 M of sodium carbonate (Na_2CO_3) solution was prepared in 150 ml of DI water and gradually added dropwise to the above solution to obtain the co-precipitates and stirred continuously. Ammonia was used to adjust the pH of the solution in a range of 7-8. Afterward, the resultant precipitate was filtered, washed several times with ethanol and DI water, and subsequently dried at 120 °C for 12 h. The dried sample was ground into a fine powder and sintered at 750 °C for 4 h at a heating rate of 4 °C min^{-1}, resulting in a homogeneous $Cu_{0.1}Sm_{0.1}Ce_{0.8}O_2$ powder for further physical and electrochemical characterizations.

Similarly, other compositions ($Cu_{0.05}Sm_{0.15}Ce_{0.8}O_2$ and $Cu_{0.15}Sm_{0.05}Ce_{0.8}O_2$) were prepared for physical and electrochemical characterizations. Preparation of several compositions help to organize and recognize the optimal composite electrolyte and then further physically and electrochemical characterized for fuel cell application.

2.2. Fuel cell device fabrication

The fuel cell was constructed with a three-layer configuration: anode, cathode, and electrolyte membrane. $Ni_{0.8}Co_{0.15}Al_{0.05}LiO_2$ (NCAL) was used as symmetric electrodes and NCAL was obtained from Tianjin Bamo Company. NCAL was referred to as triple ion conductors due to their ability to perform both hydrogen oxidation reaction (HOR) at the anode and oxygen reduction reaction (ORR) at the cathode [19]. Initially, the NCAL electrode was prepared by making NCAL slurry in an appropriate amount of terpineol as the solvent agent and then painted onto nickel foam. The electrode was then dried for 1 h at 90 °C. Afterward, a pellet of $Cu_{0.1}Sm_{0.1}Ce_{0.8}O_2$ was prepared using a hydraulic dry-press technique. The final cell configuration was assembled by sandwiching the $Cu_{0.1}Sm_{0.1}Ce_{0.8}O_2$ powder between the two NCAL electrodes and pressing them at the pressure of 220-250 MPA. The active area of the cell was 0.64 cm, with a total cell thickness of 1.5 mm and an electrolyte thickness of 510 μm. Moreover, Ni-foam was employed to provide mechanical strength and serve as the current collector. Finally, a cell configured as Ni-NCAL/$Cu_{0.1}Sm_{0.1}Ce_{0.8}O_2$/NCAL-Ni was prepared specifically for electrochemical testing, allowing for an evaluation of its performance under controlled conditions. Similarly, cells for other prepared compositions were configured such as Ni-NCAL/$Cu_{0.05}Sm_{0.15}Ce_{0.8}O_2$/NCAL-Ni, Ni-NCAL/$Cu_{0.1}Sm_{0.1}Ce_{0.8}O_2$/NCAL-Ni, and Ni-NCAL/$Cu_{0.15}Sm_{0.05}Ce_{0.8}O_2$/NCAL-Ni and tested under identical conditions. For electrochemical performance measurements, the IT8511A+ DC electronic load (150 V/30 A/150 W) by ITECH was used, with measurements conducted under standard fuel cell conditions. For electrochemical impedance spectroscopy (EIS) measurements, Solartron Energy Lab XM's impedance potentiostat was utilized. The flow rate of hydrogen and oxygen was 120 ml min^{-1}.

To investigate proton conduction, a five-layer cell configuration was developed incorporating $BaZr_{0.9}Y_{0.1}O_3$ (BZY) as a protonic conductor. This design features BZY layers strategically positioned on both sides of the electrolyte membrane such as $Cu_{0.1}Sm_{0.1}Ce_{0.8}O_2$. BZY is well known for effectively blocking oxygen and electron transport, facilitating selective proton conduction only [20]. Each layer was carefully processed to optimize interfacial quality and adhesion to maintain five layered configurations of Ni-NCAL/BZY/$Cu_{0.1}Sm_{0.1}Ce_{0.8}O_2$/BZY/NCAL-Ni. A similar methodology was applied to other prepared compositions of $Cu_{0.05}Sm_{0.15}Ce_{0.8}O_2$ and $Cu_{0.15}Sm_{0.05}Ce_{0.8}O_2$.

For the distribution relaxation time (DRT) analysis of the $Cu_{0.1}Sm_{0.1}Ce_{0.8}O_2$ membrane, NCAL electrodes were prepared using the previously described brush-coating method. Approximately 0.2 g of $Cu_{0.1}Sm_{0.1}Ce_{0.8}O_2$ powder was used to assemble the cell in a Ni-NCAL/$Cu_{0.1}Sm_{0.1}Ce_{0.8}O_2$/NCAL-Ni configuration via dry pressing. The assembled cell was heated to 550 °C for 45 min to activate the cell and air was introduced at both sides of the cell (at 520 °C) to stabilize the environment for the initial measurements. EIS measurements were conducted using a symmetrical cell configuration (NCAL/CSC/NCAL) fabricated via uniaxial pressing at 250 MPa. Measurements were performed using a Solartron 1260 impedance analyzer, covering a frequency range from 0.1 Hz to 1 MHz with an AC signal amplitude of 10 mV. A reducing hydrogen atmosphere (flow rate: 30 ml min^{-1}), and air (flow rate: 30 ml min^{-1}) was maintained, ensuring stable operating conditions. Each measurement was conducted initially in air-air environment followed by proton injection at the anode side to take repeated measurements after 10 min each. The DRT was calculated using an open-source MATLAB-based algorithm designed

for high-resolution impedance data analysis. Tikhonov regularization was employed with the regularization parameter ($\lambda = 10^{-3}$) optimized using the L-curve method, balancing fitting accuracy and noise suppression. The frequency range (0.1 Hz - 1 MHz) was chosen for DRT analysis based on observed relaxation processes in grain boundary, and interfacial regions. Peaks in the relaxation spectrum were assigned to specific electrochemical processes based on characteristic time constants and validated with existing literature. Peak fitting was cross-checked to ensure consistency in extracted parameters. Impedance spectra were pre-processed using ZSim software to eliminate any outlier noise, and MATLAB-based scripts were utilized for DRT computation and visualization. The key outputs included Relaxation peak positions, representing grain boundary and mass transfer resistance contributions. Quantified resistances extracted from the DRT and compared across different compositions.

Furthermore, the fuel cell was also configured for Hebb–Wagner DC polarization studies with a similar setup, following the same protocol used for electrochemical performance measurements. Initially, the prepared cell was activated at 550 °C for 45 min. Afterward, hydrogen was introduced at a rate of 120 ml $\min^{-1}$ alongside air, replicating the conditions of a fuel cell for proper activation of the electrolyte membrane. After 15 min, the gases were replaced with nitrogen. The experimental procedure began after another 15 min (at 520 °C) in the nitrogen atmosphere, during which 1500 data points were collected over approximately 30 min. This methodology was consistently applied to all other compositions.

Besides, conductivity calculations were conducted to investigate the electronic as well as ionic conductivity in the prepared compositions using different experimental setups. For EIS data, total conductivity was derived from the equation $R_t = R_0 + R_1$, where R_t represents the total resistance, R_0 is the ohmic resistance, and R_1 is the grain boundary resistance [21]. To assess changes in ionic conductivity over time in the DRT experiment, the formula $\sigma = L/RA$ was applied, where L represents the measured thickness of the prepared cell, and RA denotes the resistance measured in Ω cm^2. Additionally, ionic and electronic conductivities were determined from the DC polarization curves corresponding to each composition. The DC polarization conductivity was calculated using Ohm's law, which relates current (I), voltage (V), and conductivity as follows:

$$\sigma = \frac{L \times I}{A \times V}$$

where σ is the DC polarization conductivity and L is the thickness of the cell, and I is the current. A is the cross-sectional area of the sample and V is the applied voltage.

The ionic conductivity was determined through the analysis of current-voltage (*I-V*) and current–power (*I-P*) curves, which provide insights into ion transport efficiency across the electrolyte material. Initially, the *I-V* analysis was used to calculate the total resistance by determining the slope of the linear region, using Origin software [22, 23]. This resistance is inversely related to conductivity. The *I-V* curve was analyzed for each composition under H$_2$-Air atmosphere

at varying temperatures to determine the ionic conductivity. The *I-P* curve further complements this analysis by correlating power output to charge carrier mobility. This relationship helps in identifying optimized ion transport pathways and validating the efficiency of ionic conduction, supporting the overall performance of the electrolyte material.

2.3. Physical and electrochemical characterization

The synthesized materials underwent a comprehensive characterization using several techniques to evaluate their structural and morphological properties, along with the determination of co-doping effect on the band gap. Powder x-ray diffraction (XRD) was conducted by using a PANalytical Empyrean diffractometer scanning between 10° to 90° 2θ at a rate of 0.02° per second, Cu Kα radiation ($\lambda = 1.5418$ Å). The XRD patterns were analyzed using X'Pert High Score and JADE software to confirm the crystalline structure and the presence of a single-phase solid solution. Raman spectroscopy was performed using a Renishaw in Via Raman microscope to analyze the F$_{2g}$ band associated with the cubic fluorite structure of ceria (CeO$_2$). This band reflects the symmetric stretching of oxygen ions in the lattice. By examining the F$_{2g}$ band, we aimed to assess the structural changes resulting from doping with various elements. The Raman spectra were recorded at a wavelength of 532 nm and at a power of 10 mw to avoid thermal degradation of the samples. Changes in the position and intensity of the F$_{2g}$ band provide insights into the effects of doping on ceria's vibrational characteristics and can indicate alterations in ionic and electronic transport properties. Morphological and compositional characteristics were examined using field emission scanning electron microscopy (FE-SEM) supplemented by energy-dispersive x-ray spectroscopy (EDS) for detailed elemental analysis.

For surface composition and chemical state analysis, x-ray photoelectron spectroscopy (XPS) was utilized. This analysis was performed with a Thermo Fisher Scientific K-Alpha+ system, which operates in parallel data acquisition mode, employing monochromatic Al Kα radiation ($h\nu = 1486.68$ eV) with a 400 μm spot size. A high-purity, sputter-cleaned silver sample, known for its 3d5/2 binding energy of 352 eV, was used to calibrate the energy scale within the concentric hemispherical analyzer. The raw XPS data were processed with linear background subtraction before assessing individual spectral weights. Gaussian peak fitting was applied to resolve overlapping peaks. XPS was used to investigate the surface chemical states, Ce^{3+} and Ce^{4+} ratios, and the formation of oxygen vacancies. The raw XPS data were analyzed using XPSPEAK41 XPS software. UV-Vis absorption spectroscopy was also employed to determine the optical band gap of the materials employing a Perkin Elmer Lambda 950 spectrophotometer across a wavelength range of 250-1000 nm. High-resolution transmission electron microscopy (HRTEM) was employed to observe the microstructure and morphology of the 10-CSC and SDC materials. HRTEM images were analyzed to evaluate grain size, boundary formation, and structural stability. Additionally,

electron paramagnetic resonance spectroscopy was utilized to investigate the presence of defects, particularly oxygen vacancies, and to assess the electronic environment of copper ions in the material. Both techniques provided valuable insights into the structural and electronic properties of the CSC electrolyte, enhancing the understanding of its ionic conductivity and long-term stability.

3. Results and discussion

3.1. Morphological and structural characterization

Four compositions SDC, $Cu_{0.05}Sm_{0.05}CeO_2$ (5-CSC), $Cu_{0.1}Sm_{0.1}CeO_2$ (10-CSC), and $Cu_{0.15}Sm_{0.05}CeO_2$ (15-CSC)) reveal distinct differences in their structural and morphological properties due to strategically introducing various content of Cu and Sm in a periodic manner. XRD analysis was performed to investigate the co-doped ceria electrolyte's crystalline structure and phase purity. XRD data for all compositions were analyzed using retrieved refinement via Full proof software to determine structural parameters and phase composition. The results of the Sm–Cu co-doped CeO_2 reveal that the material maintains the cubic fluorite structure, similar to pure CeO_2 for all prepared compositions as evident from figure 1(a) for SDC, 5-CSC and 10-CSC compositions, where supplementary data figure S(1) shows retrieved refinement for 15-CSC composition [24]. The diffraction peaks mainly correspond to reflections from the (111), (200), (220), (311), (222), (400), (331), (420), and (422), confirming the preservation of the basic ceria structure [24, 25]. Notably, slight peak shifts are observed due to the incorporation of Sm^{3+} and Cu^{2+} into the ceria lattice. These shifts can be attributed to lattice expansion resulting from the substitution of Ce^{4+} by ions of different radii, with Sm^{3+} having a slightly smaller ionic radius than Ce^{4+} and Cu^{2+} being even smaller [26]. Further analysis of the XRD data shows that there are no additional phases, indicating that both samarium and copper are successfully incorporated into the ceria matrix without forming separate oxide phases for all prepared compositions. The slight broadening of the peaks may be related to the formation of defects such as oxygen vacancies or the introduction of micro-strain into the lattice [27]. This defect chemistry, induced by co-doping, plays a critical role in improving the material's electrochemical performance, especially for applications in SIMFCs.

Moreover, Raman spectroscopy of $Sm_{0.2}Ce_{0.8}O_2$ revealed the characteristic F_{2g} vibrational mode around 462 cm^{-1}, corresponding to the symmetric stretching of the Ce-O bond [26]. Doping with copper led to a slight shift of this band to lower wavenumbers, measured at 460.69 cm^{-1} for $Cu_{0.05}Sm_{0.15}CeO_2$, reflecting lattice distortion due to the incorporation of dopants and the associated oxygen vacancies, as shown in figure 1(b). Interestingly, a further increase in copper concentration stabilized the Ce-O vibrations, shifting them slightly back to 462.62 cm^{-1}, while significantly increasing the peak intensity, indicating enhanced structural stabilization and defect formation. The Raman spectra for co-doped compositions also exhibited additional broad bands in the range of 550-600 cm^{-1}, attributed to defect-related vibrations caused by oxygen vacancy clusters [14]. The progressive increase in the intensity of these defect bands with higher copper doping highlights the role of copper in promoting oxygen vacancy formation, which is critical for ionic conduction. These defect-related vibrational modes, absent in the SDC composition, underscore the significant role of copper as a co-dopant in the SDC matrix, not only in generating oxygen vacancies but also in facilitating enhanced ionic transport pathways. This improvement in defect concentration and lattice structure directly correlates with the observed increase in ionic conductivity and reduced grain boundary resistance, as evidenced by EIS analysis. FE-SEM was employed to observe the morphology of Sm-Cu co-doped CeO_2 compositions. It can be seen that spherical and less interacted particles can be observed in SDC shown in figure 1(c) As copper is introduced into the system, it forms a more interlinked particle structure which increases as copper concentration increases in the compositions as evident from figures 1(d) and (f). Figure 1(e) shows $Cu_{0.1}Sm_{0.1}CeO_2$ composition which exhibits the most uniform and interlinked particle structure morphology, with a nanorods-like structure. The $Cu_{0.1}Sm_{0.1}CeO_2$ creates an optimized microstructure that minimizes agglomeration and enhances the surface area, which is crucial for improving ionic conductivity. In comparison, the $Cu_{0.05}Sm_{0.15}CeO_2$ and $Cu_{0.15}Sm_{0.05}CeO_2$ compositions show less homogeneity in particle size distribution, with some larger clusters present, which can negatively affect ionic transport efficiency as evident from figures 1(d) and (f). For the comparison of EDX mapping results along with elemental mapping analysis for all compositions as provided in supplementary data figure S2(x-z), the $Cu_{0.1}Sm_{0.1}CeO_2$ composition shows the most uniform distribution of Cu, Sm, and Ce, with no signs of phase separation or clustering of the dopants. This homogeneity is crucial for ensuring consistent ionic and electronic conductivity throughout the material. The even dispersion of Cu and Sm within the ceria matrix highlights the success of the co-precipitation method in achieving controlled doping. In contrast, the $Cu_{0.05}Sm_{0.15}CeO_2$ and $Cu_{0.15}Sm_{0.05}CeO_2$ compositions show less uniform elemental distributions.

Figure 1(e) shows that $Cu_{0.1}Sm_{0.1}CeO_2$ sample displays relatively more interconnected and fibrous morphology that could be beneficial for ionic conductivity by facilitating ion transport through these interlinked pathways. The fibrous morphology observed in this image may improve catalytic properties and ionic mobility by creating channels that allow ions to move with less resistance, a factor crucial for electrolyte applications [28]. This analysis demonstrates that the Sm^{+3} and Cu^{+2} co-doping ceria lattice induces beneficial morphological modifications, which are crucial for enhancing the functionality of ceria-based electrolytes in fuel cell devices. Moreover, the combination of XRD and Raman results provides strong evidence for the successful integration of dopants, the preservation of the fluorite structure, and the crucial role of oxygen vacancies in enhancing the material's conductivity.
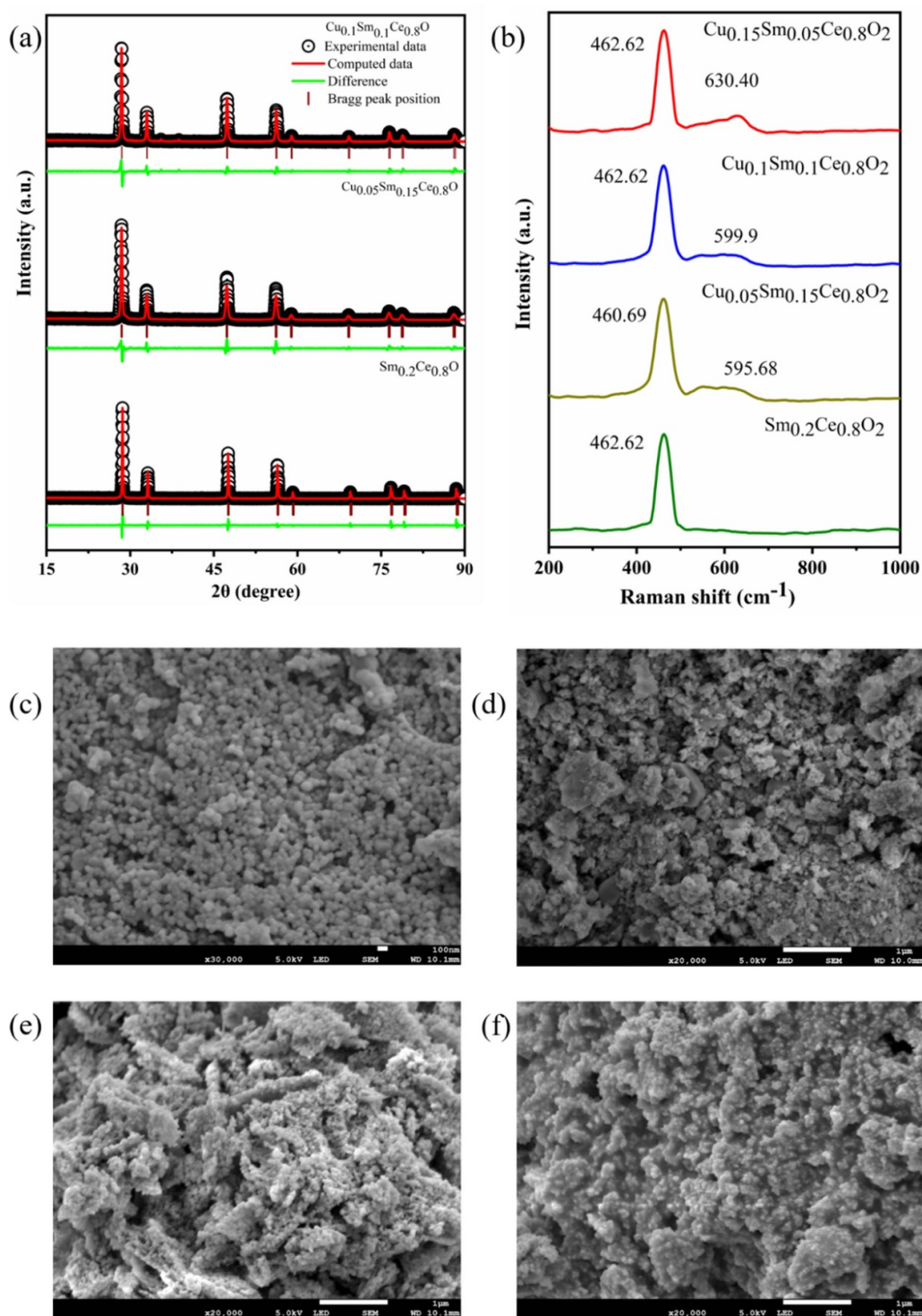
Figure 1. X-ray diffraction (XRD) patterns with retrieved refinement via full proof software, showing the structural parameters and phase composition for each sample of SDC, 5-CSC, and 10-CSC compositions (a), Raman spectra for respective compositions of CSC, 5-CSC, 10-CSC and 15-CSC (b), and scanning electron microscopy images of SDC (c), 5-CSC (d), 10-CSC (e), 15-CSC (f).

3.2. Surface and chemical oxidation state study

The XPS analysis provides insightful details regarding the surface and chemical states of the respective compositions, particularly focusing on the O-1s, Ce-3d, and overall elemental survey spectra [29]. For the four compositions (SDC, $Cu_{0.05}Sm_{0.15}CeO_2$, $Cu_{0.1}Sm_{0.1}CeO_2$, and $Cu_{0.15}Sm_{0.05}CeO_2$), the analysis reveals key distinctions that highlight $Cu_{0.1}Sm_{0.1}CeO_2$ as the most promising composition. The survey spectra confirm the presence of Ce, Sm, Cu, and O in all compositions as shown in figure S3. This analysis specifically focuses on the Ce-3d, Cu-2p, Sm-3d, and O-1s spectra to elaborate and understand the impact of Cu and Sm

doping on the electronic structure, and vacancy formation, and assist in determining oxidation states of Cu and Sm, which assure the mixed ionic-electronic conductivity (MIEC). The Ce-3d spectrum in Cu-Sm co-doped CeO_2 is composed of a different set of peaks representing the Ce^{4+} and Ce^{3+} oxidation states. The spectrum is divided into two primary multiples, labeled V (Ce-$3d_{5/2}$) and U (Ce-$3d_{3/2}$), corresponding to spin–orbit split final states in the Ce-3d core level [30]. These multiplets are further divided into distinct peaks. The presence of Ce^{4+} characteristic peak in SDC at high binding energy peaks, particularly u‴ and v‴, which correspond to the final electronic configuration Ce $3d^9$ $4f^0$ O_2P^6; [31]. These peaks are strong indicators of Ce^{4+}, which are predominant in SDC. Additional lower binding energy peaks in the Ce-3d spectrum in SDC, namely u, v, u″, and v″, correspond to configurations Ce $3d^9$ $4f^2$ O_2P^4 and Ce $3d^9$ $4f^1$ O_2P^5, associated with Ce^{4+} states [32]. Moreover doping with Cu and Sm alters the CeO_2 electronic structure by promoting the partial reduction of Ce^{4+} to Ce^{3+}. In the $Cu_{0.1}Sm_{0.1}CeO_2$ sample, additional peaks labeled u_0, u′, and v′ which are indicative of Ce^{3+} states are more prominent than in SDC, 5-CSC, and 15-CSC, depicted in figures 2(a) and (b). These peaks present the final state configuration of Ce $3d^9$ $4f^1$, which are characteristics of Ce^{3+} oxidation state. Thus, the presence of Cu and Sm dopants induces slight shifts in the binding energies of the Ce-3d spectrum. These shifts reflect local distortions in the CeO_2 lattice [33] which facilitated the formation of oxygen vacancies by altering the electronic environment of Ce atoms. The enhanced fraction of Ce^{3+} correlates directly with an increase in oxygen vacancies, as Ce^{3+} sites stabilize these vacancies within the matrix, ultimately promoting ionic conduction pathways in the co-doped ceria structure [34]. Moreover the Cu-2p spectra reveal the oxidation state of copper within the Cu-Sm-CeO_2 structure, showing both Cu^+ and Cu^{2+} states. Peaks at around 932 eV (Cu-$2p_{3/2}$) and around 952 eV (Cu-$2p_{1/2}$) are indicative of Cu^+, while satellite peak near 940 eV and 962 eV suggest a partial Cu^{2+} state [35] as shown in figure S4(a). Cu^+ enhances oxygen vacancy formation, while Cu^{2+} contributes to electronic conduction, creating a MIEC conducive to applications in electrochemical systems [36]. Afterward, the Sm-3d spectrum shows peaks at around 1081 eV for Sm-$3d_{5/2}$ and around 1108 eV for Sm-$3d_{3/2}$, indicating that Sm exists predominantly as Sm^{3+} in the co-doped sample as shown in figure S4(b). Sm^{3+} doping is crucial as it stabilizes oxygen vacancies in the ceria matrix and facilitates ionic transport by enhancing vacancy mobility. Additionally, Sm^{3+} doping leads to lattice expansion, which accommodates oxygen vacancies, aiding ionic conduction within the material [11].

The combined effect of Cu and Sm doping in CeO_2 increased oxygen vacancy concentrations simultaneously and significantly, as evidenced by the pronounced Ov peak in figures 2(c)–(f). The XPS O-1s spectra were deconvoluted into 3 different peaks: O_{Latt}, O_{Vac}, and O_{Abs}. Table 1 provides the lattice oxygen, oxygen vacancies, and surface absorbed at respective binding energies for each prepared composition. The binding energies of lattice oxygen, oxygen vacancies, and surface absorbed in SDC are at the lower side for all respective

combinations. While with the incorporation of Cu, a noticeable shift in binding energies occurs towards higher binding energies. Furthermore, $Cu_{0.1}Sm_{0.1}CeO_2$ composition generates the highest surface-related oxygen vacancies (56.6%) compared to compositions due to the mixed-valence copper (Cu^+/Cu^{2+}), which introduces both pathways, such as Cu^+ promoting vacancy formation while Cu^{2+} enhancing electronic pathways. This combination of ionic and electronic conduction mechanisms in the optimized CSC compositions assists in the improvement of electrochemical performance for low-temperature fuel cell applications [37]. Recent studies demonstrated that GDC has been favored for enhancing ionic conductivity due to Gd^{3+}-induced oxygen vacancies [10]. However, CSC compositions provide higher oxygen vacancy concentrations attributed to the dual doping strategy, which offers synergistic effects between Cu^+ and Sm^{3+} as denoted in figures 2(c)–(f) and table 1. This dual doping enhances oxygen ion mobility and stabilizes vacancies more effectively than single-dopant systems, making Cu-Sm-CeO_2 more suited for high ionic conduction. Unlike single-doped ceria, CSC compositions exhibit MIEC due to Cu^+ and Cu^{2+} redox activity. Literature reports and suggests that Sm doping alone can enhance the thermal stability of ceria [38, 39], while Cu doping promotes redox reactions [40]. Comparative analyses with Nb-doped ceria reveal that while Nb doping increases electronic conductivity, but lacks the capability of vacancy formation efficiency, resulting in lower ionic conductivity in comparison [41]. Hence, the increased oxygen vacancy concentration facilitates ionic conduction, while Cu^+/Cu^{2+} states introduce electronic pathways, yielding a MIEC.

3.3. UV-visible spectroscopy

Copper, being an electronic conductor, naturally introduces electronic states that can facilitate electron properties. In systems like Cu-doped ceria, electronic conductivity is indeed expected to increase due to the presence of Cu, which contributes additional electronic states within the material's structure but it cannot be simply considered an electronic conducting material. Moreover, the behavior of the band gap in Cu-Sm ceria co-doped (CSC) systems does not simply reflect the presence of copper alone but also the interaction between ions of copper, samarium, and cerium. Thus, we employed UV-Vis spectroscopy to dugout the semiconducting properties of Sm-Cu co-doped CeO_2, where the band gap of semiconductor materials can be tuned by doping [42]. The Tauc plot of UV-Vis spectroscopy provides the band gap variations across the compositions as shown in figures 3(a)–(d). It can be seen in figures 3(a) and (b) that with the introduction of Cu, the band gap reduced from 3.12 to 2.93 eV because Cu has the capability to introduce certain electronic characteristics, which can reduce the band gap by bringing valance band levels closer to the conduction band. However, in $Cu_{0.1}Sm_{0.1}CeO_2$, a smaller reduction in band gap is observed such as 3.13-2.93 eV, which is possible due to the balance between the doping ratio of Sm and Cu and also their respective optimized contribution of ionic and electronic characteristics. This modest tuned band
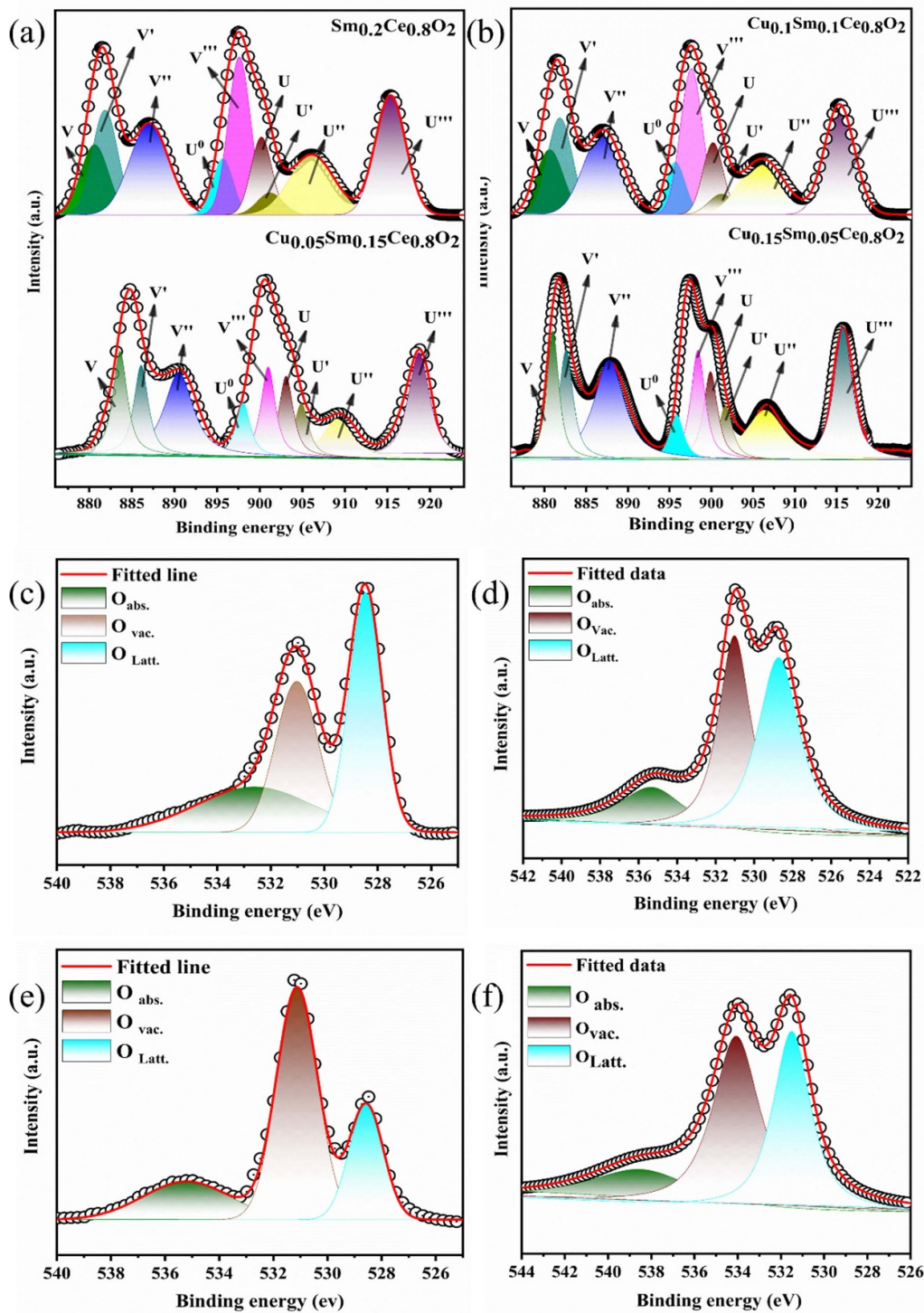
Figure 2. XPS spectrum of Ce-3d spectrum for SDC and 10-CSC composition (a), Ce-3d of 5-CSC and 10-CSC composition (b), O-1s spectra of SDC (c), 5-CSC (d), 10-CSC (e), 15-CSC (f).

gap of 3.04 eV of $Sm_{0.1}Cu_{0.1}Ce_{0.8}O$ shows a balance between electronic and ionic conductivity [43]. This band gap allows for controlled electronic conduction without compromising ionic pathways, which is essential for efficient ionic transport in SIMFCs. This balance between controlled ionic and electronic conduction improved the ionic transport by the formation of built-in electric field, which makes $Cu_{0.1}Sm_{0.1}CeO_2$

a superior composition for SOFCs, which will be discussed later. Similarly, For $Cu_{0.15}Sm_{0.05}CeO_2$ composition, the calculated bandgap is 3.06 eV. This increase in bandgap after increasing the dopant concentration is in accordance with the previously reported literature [44]. Therefore, it may be suggested that $Cu_{0.1}Sm_{0.1}CeO_2$ represents an optimized balance, which can be evident in the electrochemical performance of

Table 1. Binding energies for lattice oxygen, oxygen vacancies, and surface absorbed for each prepared composition along with oxygen vacancy ratio.

	SDC	5-CSC	10-CSC	15-CSC
O_{Latt}	528.4	531.5	528.5	528.7
O_{vac}	531.1	534.1	531.1	531.1
$O_{Surface\ absorbed}$	532.6	538.5	535.1	535.4
Vacancy ratio	32.2%	46.6%	56.6%	42%
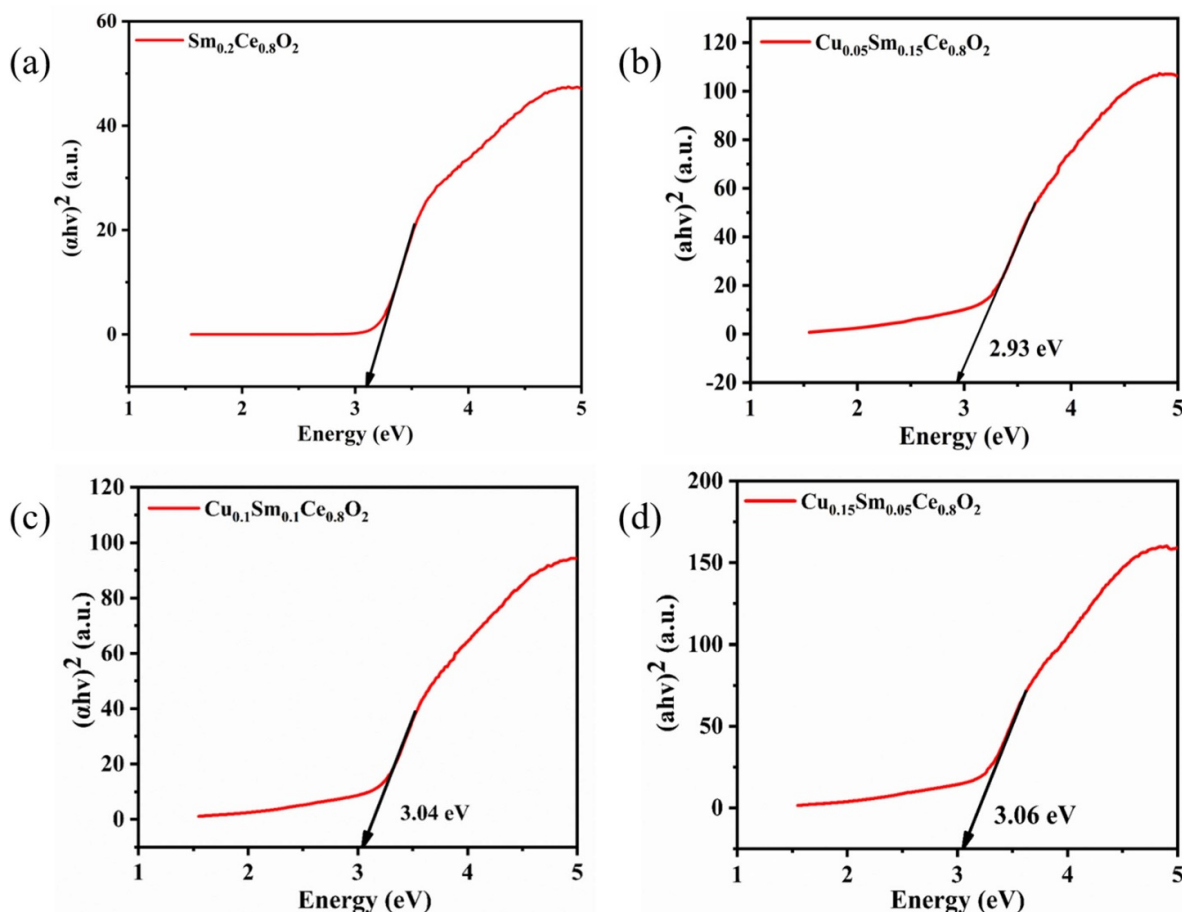
Figure 3. Obtained band gap from the absorbance of UV-Vis graphs SDC (a), and 5-CSC (b), 10-CSC (c), and 15-CSC (d).

the fuel cell device constructed based on various designed materials system.

3.4. Microstructural analysis

The HR-TEM analysis for SDC (figures 4(a)–(f)) reveals a predominantly spherical morphology with uniform and well-defined grains, reflecting the stable, compact structure typical of single-doped ceria. Figures 4(a)–(c) at 200 nm, 100 nm, and 50 nm show well-defined and more uniform grains, characteristic of a single-dopant system, with grain size averaging 48.56 ± 1.37 nm in size (calculated from figure 4(b), represented in figure 4(n)). The grain boundaries in SDC are visible but relatively smooth, indicating low defect density in the material. This stable and uniform crystalline structure is favorable

for maintaining consistent ionic conductivity, though the lack of significant grain boundary density limits enhanced ion transport pathways. This uniformity underscores the homogeneous crystalline structure of SDC.

In contrast, 10-CSC (figures 4(g)–(i)) shows a notable change in morphology, with the particles adopting a cubical shape illustrating the more fragmented particles through 200 nm, 100 nm, and 50 nm magnification, respectively, with grains averaging 26.10 ± 0.50 nm in size (calculated from figure 4(h), represented in figure 4(m)). The increased surface area and more fragmented particle structure in 10-CSC are indicative of the structural modifications induced by copper co-doping, which alters the nucleation and growth dynamics during synthesis. The 5 nm scale bars in figures 4(f)–(l) further emphasize the reduction in crystallite size and the
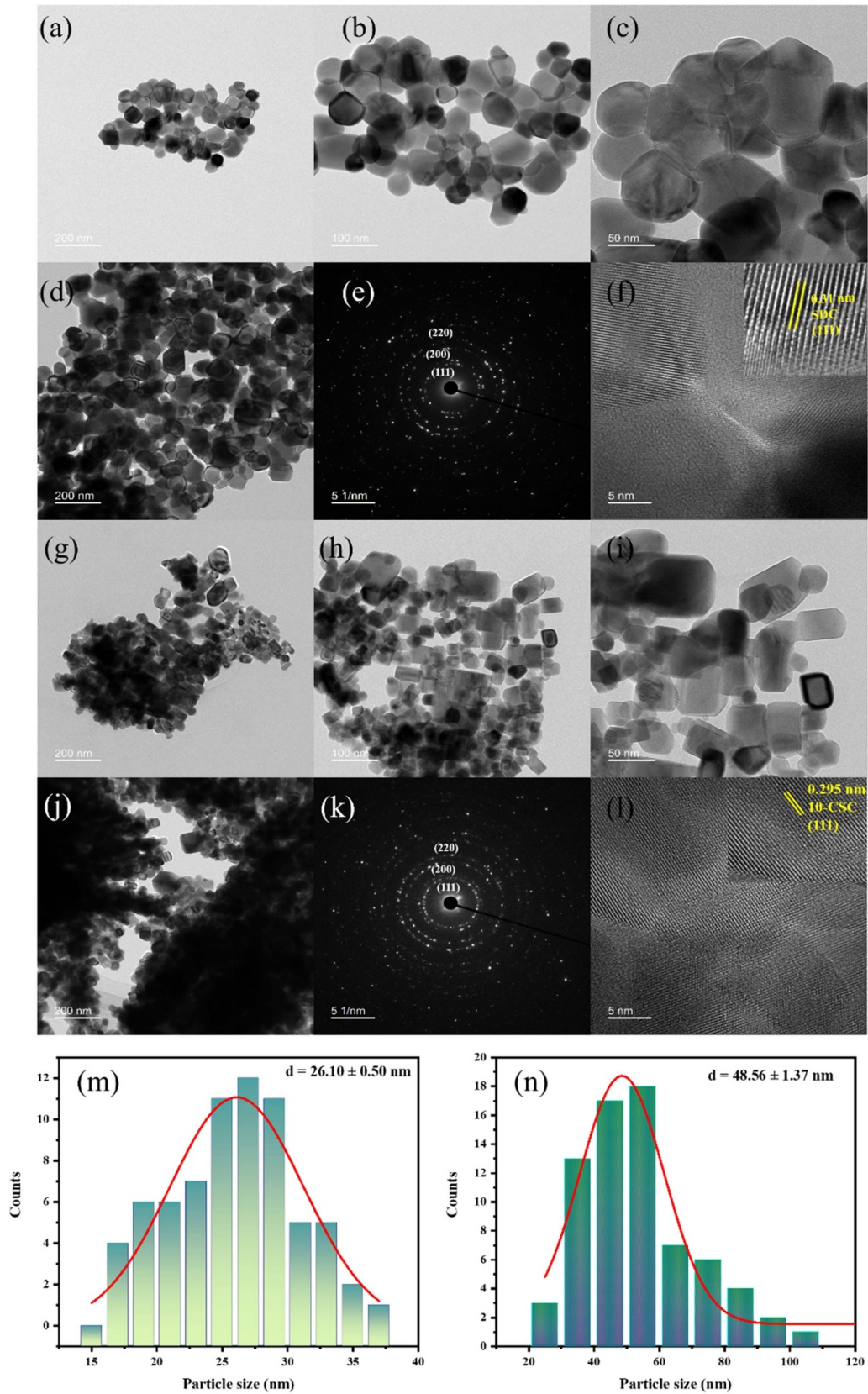
Figure 4. TEM images of SDC (a)–(f), and 10-CSC (g)–(l), at different magnifications illustrate particle morphology and agglomeration. The SAED patterns for SDC (e), and for 10-CSC (k), confirm the crystalline nature, while HR-TEM images (f) for SDC, and (l) for 10-CSC, reveal clear lattice fringes, indicating structural integrity. Particle size analysis (m) for 10-CSC, and (n) for SDC shows an average size of 26.10 ± 0.50 nm and 48.56 ± 1.37 nm for 10-CSC and SDC, respectively.

morphological shift. These observations indicate that copper co-doping alters the nucleation and growth dynamics, leading to smaller particles with higher surface area.

Regarding grain boundaries, while they are not as sharply defined in 10-CSC compared to SDC, the overall grain boundary density is higher due to the smaller grain size and more disordered lattice as evident from figures 4(f)–(l). The increased disorder at the grain boundaries, visible in the HR-TEM images, is attributed to the lattice distortions introduced by copper, which enhances oxygen vacancy formation and increases the material's defect density. This is further confirmed by the lattice spacing of 0.295 nm for 10-CSC and 0.31 nm for SDC (inset figures 4(f)–(l)) aligns with HRTEM and selected area electron diffraction (SAED) patterns observations. These structural changes are crucial for improving ionic conductivity, as the greater boundary density provides additional pathways for ion transport. The SAED patterns support these findings. The SAED pattern for SDC (figure 4(e)) shows distinct, sharp diffraction spots, indicating a predominantly crystalline structure with low defect density. In contrast, the SAED pattern for 10-CSC (figure 4(k)) exhibits broader, weaker diffraction spots, suggesting lattice distortions and reduced crystallinity due to more diffused grains. This broadening is consistent with the increased concentration of defects and oxygen vacancies in 10-CSC, which contribute to smaller crystallites and enhanced ionic conductivity by creating more grain boundary pathways for ion transport.

The SEM images presented (figures 1 (c) and (e)) clearly illustrate significant differences in the grain morphology and size distribution between SDC and10-CSC samples where SDC (figure 4(c)) shows a compact structure with relatively larger and uniform grain sizes. In contrast, the 10-CSC image (figure 4(e)) reveals a highly fragmented morphology with smaller grain size. This reduction in grain size directly correlates with the enhanced grain boundary density observed in the HRTEM images. The combined use of HRTEM, SAED, and SEM analyses provides unequivocal evidence that copper co-doping into SDC results in significant structural changes, including grain size reduction, morphological transformation, and an increase in grain boundary density. These modifications directly contribute to the enhanced ionic conductivity of 10-CSC, crucial for its improved electrochemical performance.

3.5. Electrochemical characterizations

The EIS analysis of fuel cell devices based on various compositions were conducted to understand their electrochemical behavior in a temperature range from 520 °C to 320 °C. This technique helps to isolate the contributions of bulk (R_0), interfacial/grain boundary (R_1), and polarization resistance (R_2) components to the total resistance (R_t) of the material using an equivalent circuit of the form $R_0(R_1\text{-}QPE_1)$ $(R_2\text{-}QPE_2)$ enabling a detailed analysis of its ionic and electronic conduction properties [21]. Table 2 provides a detailed analysis in terms of R_0, R_1, R_2, and R_t for all prepared compositions at the complete testing temperature range. Here R_t represents total resistance, measured as the sum of both R_0 and R_1 formulated

Table 2. EIS simulated data for SDC and CSC compositions; where the resistance is denoted by Ω cm^2.

Temperature (°C)	R_0	R_1	R_2	$R_T = R_0 + R_1$
$Sm_{0.2}Ce_{0.8}O_2$				
520	0.12	0.09	0.32	0.21
470	0.15	0.12	0.34	0.27
420	0.18	0.16	1.04	0.34
370	0.22	0.25	8.03	0.47
$Cu_{0.05}Sm_{0.15}CeO_2$				
520	0.07	0.05	0.23	0.12
470	0.09	0.08	0.32	0.17
420	0.12	0.12	0.87	0.24
370	0.17	0.21	1.75	0.38
$Cu_{0.1}Sm_{0.1}CeO_2$				
520	0.055	0.035	0.20	0.09
470	0.08	0.06	0.26	0.14
420	0.11	0.10	0.64	0.21
370	0.15	0.18	1.70	0.33
320	0.23	0.30	11.50	0.53
$Cu_{0.15}Sm_{0.05}CeO_2$				
520	0.08	0.07	0.25	0.15
470	0.12	0.09	0.27	0.21
420	0.14	0.12	0.89	0.26
370	0.19	0.25	5.04	0.44

as ($R_t = R_0 + R_1$). The constant phase element (QPE) was introduced to account for the non-ideal capacitive behavior observed at the interfaces. This circuit model provides a good fit for the experimental data and helps to deconvolute the different resistances contributing to the overall impedance as reported in the literature [21, 45]. In the Nyquist plots, the high-frequency intercept on the real axis represents the cell's total Ohmic resistance, primarily due to the electrolyte's ionic resistance. The first semicircle at intermediate frequencies corresponds to grain boundary resistance, indicating impedance from charge transfer and ion migration across grain boundaries. The second, often larger, semicircle at lower frequencies reflects polarization resistance, which arises from electrochemical reactions at the electrode–electrolyte interface and mass transfer limitations. Analyzing the resistance characteristics various compositions of $Cu_xSm_{0.2-x}Ce_{0.8}O_2$, $x = 0$, 0.05, 0.10, 0.15, where $Cu_{0.1}Sm_{0.1}CeO_2$ has significantly lower Ohmic as well as polarization resistances as evident from figures 5(a)–(d) and table 2. At 520 °C, the EIS spectra for $Cu_{0.1}Sm_{0.1}CeO_2$ show the lowest R_0 and R_1 as well as R_2 values made it optimized composition with the least total resistance of 0.09 Ω cm^2. Another factor to notice is the bulk resistance (R_0) of 0.055 Ω cm^2 dominating over grain boundary resistance (R_1) calculated as 0.035 Ω cm^2. As the temperature decreases to 470 °C and further to 420 °C, R_1 increases, measured at 0.06 and 0.10 Ω cm^2, respectively, while bulk resistance (R_0) remains larger than R_1, as shown in figure 5(c) and table 2. This indicates that at
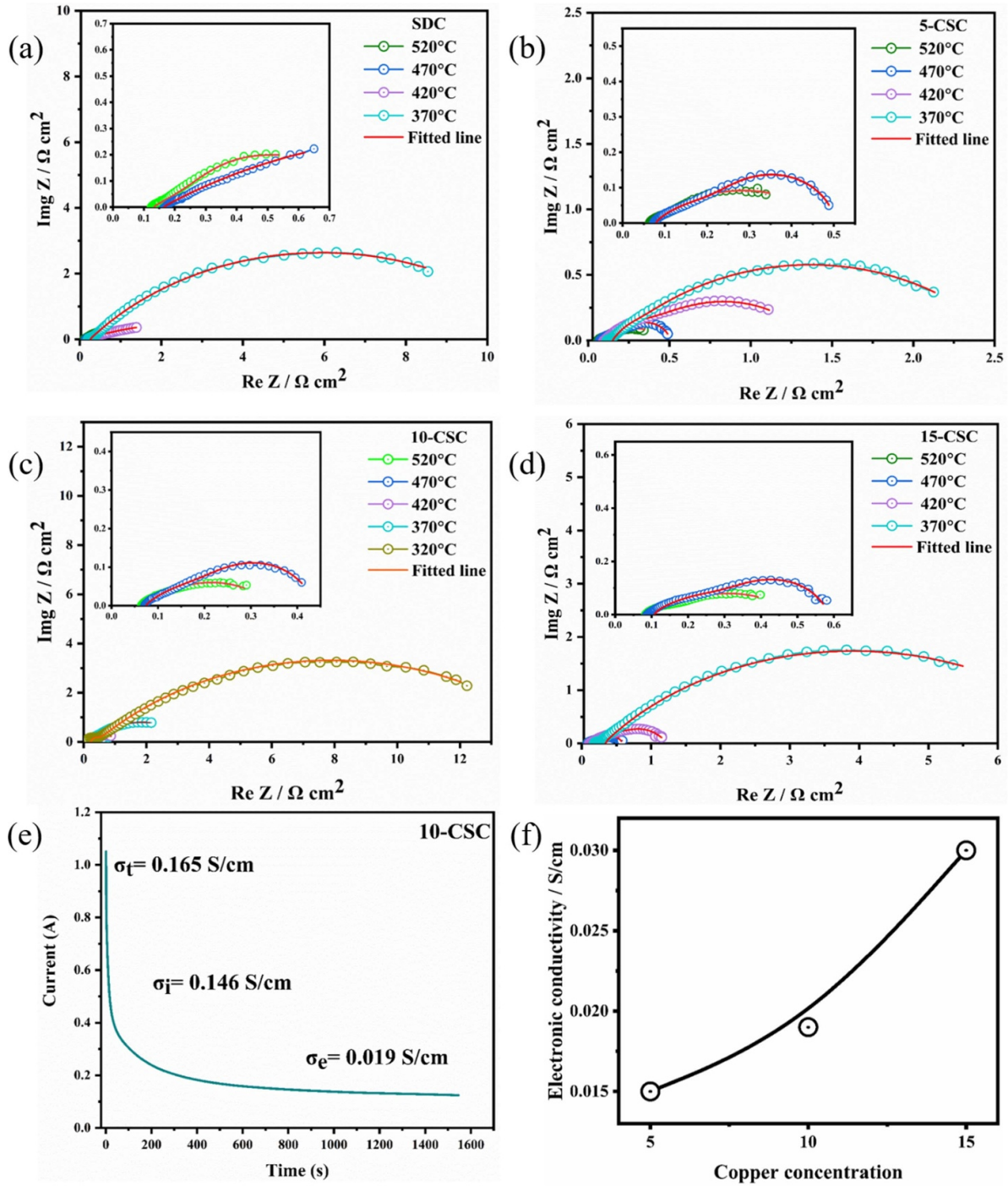
Figure 5. Electrochemical impedance spectroscopy with the simulated graph of SDC (a), 5-CSC (b), 10-CSC (c), and 15-CSC (d), DC polarization conductivity in nitrogen atmosphere for 10-CSC (e), and electronic conductivity plot against copper concentration (f).

temperatures down to 420 °C, $Cu_{0.1}Sm_{0.1}CeO_2$ predominantly exhibits grain boundary conduction, where ionic pathways along grain boundaries are more active than in the bulk material. This higher bulk resistance than grain boundary resistance above 420 °C is an expected behavior in such semiconductor ionic membrane (SIM) [23]. The microstructural features of $Cu_{0.1}Sm_{0.1}CeO_2$ also play a critical role in determining its impedance characteristics. The co-doping of Cu and Sm induced special microstructure that promotes fine grain

growth and maintains a high density of grain boundaries, which act as favorable sites for ionic transport. In solid oxide fuel cell (SOFC) electrolytes, these grain boundaries serve as highly conductive pathways for oxygen ions and protons, particularly in the presence of dopants that reduce defect formation energy and improve ionic migration [45, 46]. At higher temperatures (520 °C), grain boundary resistance is also minimized due to increased thermal activation of ion transport. As the temperature is reduced below 420 °C,

grain boundary resistance (R_1) overtakes bulk resistance (R_0). Moreover, the other compositions, such as $Cu_{0.05}Sm_{0.15}CeO_2$ and $Cu_{0.15}Sm_{0.05}CeO_2$ show more pronounced Ohmic as well as polarization resistances at lower temperatures, which contribute to their overall higher resistances, further proving the superior electrochemical properties of $Cu_{0.1}Sm_{0.1}CeO_2$ than other compositions. Further lowering the operating temperature to 370 °C and 320 °C, the bulk resistance (R_0) is increased to 0.15 Ω cm^2 and 0.23 Ω cm^2 of prepared cell based on $Cu_{0.1}Sm_{0.1}CeO_2$, resulting into reduced ionic mobility in the bulk with reduction of temperature. The introduction of optimized Cu^{2+} concentration enhances charge transfer properties by promoting redox activity, while Sm^{3+} stabilizes oxygen vacancies, creating an efficient proton conduction pathway. The combined effect reduces grain boundary resistance and facilitates a balance between ionic transport assisted by electronic transfer. Nonetheless, the grain boundary resistance remains relatively low, further demonstrating the importance of grain boundary conduction in the overall performance of the $Cu_{0.1}Sm_{0.1}CeO_2$ system.

Further consider the discussion based on polarization resistance (R_2), the values remain relatively low across the entire temperature range for $Cu_{0.1}Sm_{0.1}CeO_2$, demonstrating its superior electrochemical activity at the electrode/electrolyte interface. The low polarization resistance is crucial for reducing energy losses in the fuel cell, especially at lower operating temperatures, where charge transfer at the interface becomes more challenging [47]. When $Cu_{0.1}Sm_{0.1}CeO_2$ compared with other compositions, such as $Cu_{0.15}Sm_{0.05}CeO_2$ and $Cu_{0.05}Sm_{0.15}CeO_2$, it becomes evident that $Cu_{0.1}Sm_{0.1}CeO_2$ offers the lowest resistances, particularly at lower temperatures. For $Cu_{0.15}Sm_{0.05}CeO_2$, the grain boundary resistance, though relatively low at 520 °C (0.07 Ω cm^2), increases more steeply with decreasing temperature. This sharper rise in grain boundary resistance leads to a higher overall resistance compared to $Cu_{0.1}Sm_{0.1}CeO_2$ as the temperature drops. This suggests that $Cu_{0.15}Sm_{0.05}CeO_2$ may experience more restricted ionic transport along grain boundaries at lower temperatures, resulting in less efficient conduction than in $Cu_{0.1}Sm_{0.1}CeO_2$. This suggests that the balance between Cu and Sm doping concentrations in $Cu_{0.1}Sm_{0.1}CeO_2$ optimally enhances the electrochemical performance by providing sufficient ionic pathways while maintaining stable electronic conduction. Furthermore, at 320 °C, $Cu_{0.1}Sm_{0.1}CeO_2$ outperforms the other compositions, exhibiting a significantly lower total resistance (0.53 Ω cm^2). This result highlights the importance of co-doping in stabilizing the material's structure and enhancing ionic conductivity at lower operating temperatures, making $Cu_{0.1}Sm_{0.1}CeO_2$ a promising candidate for intermediate-temperature SOFCs (IT-SOFCs). Hence, EIS analysis reveals that $Cu_{0.1}Sm_{0.1}CeO_2$ demonstrates the best electrochemical performance among the tested compositions, owing to its favorable grain boundary conduction at intermediate temperatures, lower polarization resistance, and optimized bulk and grain boundary resistances. These findings underscore the potential of $Cu_{0.1}Sm_{0.1}CeO_2$ as a high-performance electrolyte for SOFC applications, particularly at reduced operating temperatures.

3.6. DC polarization

measurements were conducted to assess the electronic conductivity of the Sm-Cu co-doped CeO_2 compositions as depicted in figures 5(e) and (f) and supplementary data figure S6. The analysis reveals a clear trend of increasing electronic conductivity with the rise in copper content, demonstrating the role of copper as a key contributor to the material's electronic conduction properties. Here, it can be seen in $Cu_{0.05}Sm_{0.15}CeO_2$, the electronic conductivity was measured approximately 0.015 S cm^{-1}, indicating that at this lower copper content, the material retains primarily ionic conduction, with electronic conduction beginning to emerge but remaining relatively low. This suggests that at this composition, the ceria matrix is still predominantly ionically conductive, with only a minor contribution from electron transport. The electronic conduction is likely due to the formation of oxygen vacancies induced by the copper doping, which provides some degree of electron mobility through defect sites. As the copper content is increased to $Cu_{0.1}Sm_{0.1}CeO_2$, the electronic conductivity rises to 0.019 S cm^{-1}. This composition shows certain optimized ionic-electronic conductivity behavior, with electronic conduction becoming more significant. The increase in electronic conductivity with 10% of copper doping can be attributed to the enhanced availability of mobile charge carriers (electrons) as copper content increases. The material still exhibits strong ionic conduction, but the rise in electron transport improves its overall electrochemical performance, particularly in applications where mixed conduction is beneficial, such as in SIMFCs. For $Cu_{0.15}Sm_{0.05}CeO_2$, the electronic conductivity dramatically increases to 0.3 S cm^{-1}. At this higher copper content, the material exhibits much stronger electronic conduction. The significant increase in electronic conductivity can be explained by the higher concentration of copper ions within the ceria lattice, leading to more pronounced electron transport pathways. However, this comes with a trade-off as the excessive copper content may begin to suppress ionic conduction, which is less favorable and deteriorative for SOFC applications because the optimized mixed conduction is essential. Thus, based on the DC polarization results, $Cu_{0.1}Sm_{0.1}CeO_2$ emerges as the optimal composition, balancing both ionic and electronic conductivities. The 0.019 S cm^{-1} of electronic conductivity provided by this composition allows for enhanced electron transport without sacrificing ionic conduction. Therefore, $Cu_{0.1}Sm_{0.1}CeO_2$ proves to be the most suitable composition for applications requiring efficient MIEC.

3.7. Applicability of designed materials as electrolyte

To evaluate the fuel cell performance of the various Cu–Sm co-doped CeO_2 compositions, the fuel cell devices based on various compositions were evaluated in terms of *I-V* and *I-P* curves in a temperature range from 520 °C to 320 °C. Figures 6(a)–(d) shows the power outputs, OCV, and current density for various fuel cell devices based on different compositions at varying temperatures. Fuel cell based on SDC electrolyte generated power density of 502 mW cm^{-2}
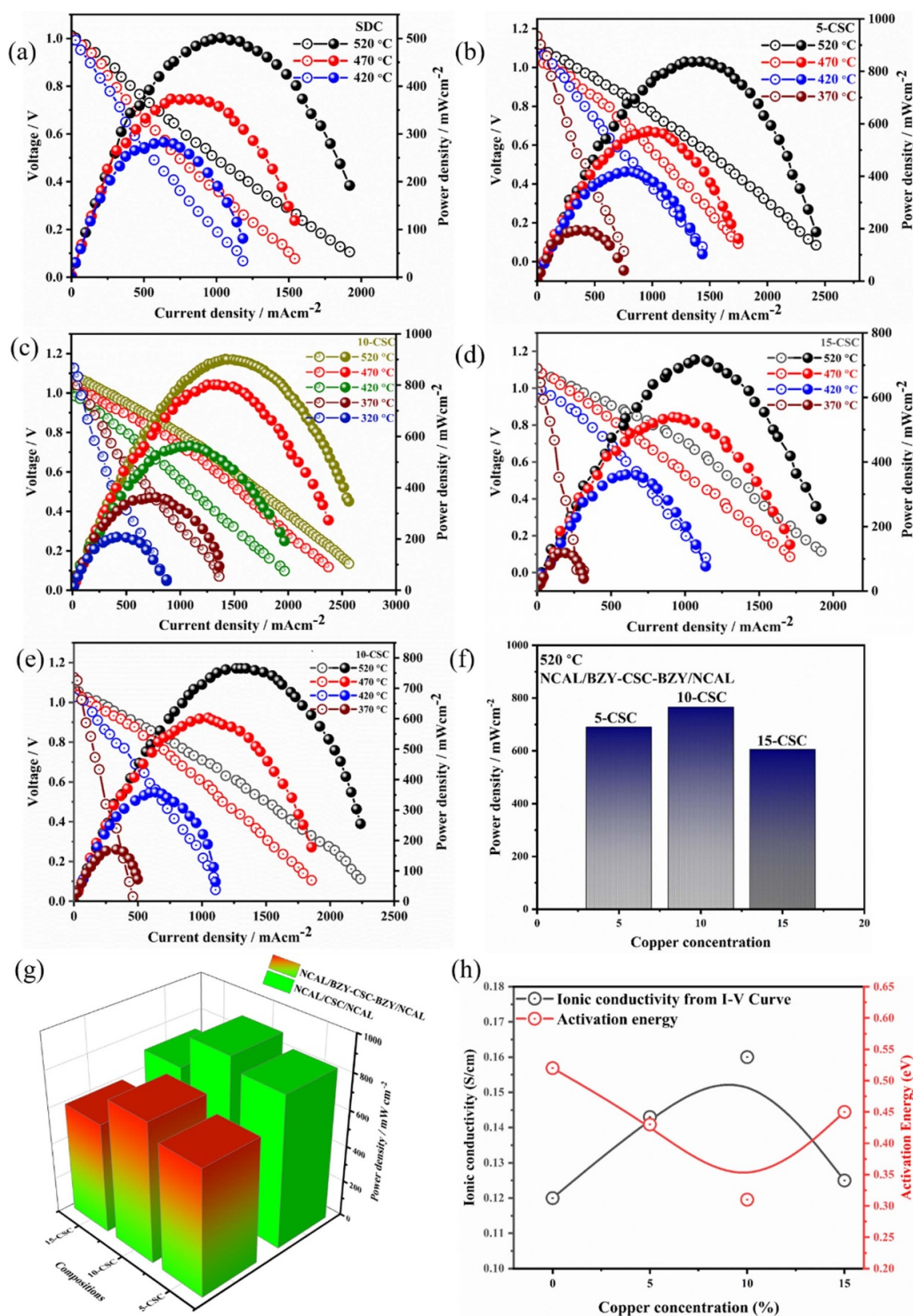
Figure 6. Fuel cell power output graphs of SDC (a), 5-CSC (b), 10-CSC (c), and 15-CSC (d) under the H$_2$/air environments. Fuel cell performance in terms of power output with five layers at different operational temperatures from 520 °C-370 °C for Ni-NCAL/BZY/10-CSC/BZY/NCAL-Ni (e), Detailed power density comparison for 5-CSC, 10-CSC, and 15-CSC at 520 °C with BZY filtered cells (f), 3D visualization of power density performance for NCAL/BZY-CSC-BZY/NCAL and NCAL/CSC/NCAL configurations, highlighting the superior electrochemical performance of 10-CSC (g). Ionic conductivity and activation energy as a function of copper concentration in CSC, showing optimal performance at 10% copper doping (h).

with 1.01 V of OCV at 520 °C, while lowering the operational temperature up to 470 °C, power density reduced further reaching the value of 375 mW cm^{-2}. Furthermore, it only provided significant power output till 420 °C, reaching the value of 282 mW cm^{-2} as shown in figure 6(a). Furthermore, the fuel cell device based on $Cu_{0.05}Sm_{0.15}CeO_2$ electrolyte demonstrated better power output of 838 mW cm^{-2} at 520 °C with higher OCV of 1.10 V, while with lowering the operational temperature, the power density reduced to 571 and 417 mW cm^{-2} at 470 °C and 420 °C, respectively. However, the performance further decreases as the temperature further drops, reaching 190 mW cm^{-2} at 370 °C as evident from figure 6(b). But the power output was relatively higher at lower temperatures compared to SDC composition due to the introduction of copper concentration, which facilitates proton conductivity via the formation of oxygen vacancies. Yet, the copper concentration is limited (5%), restricting the redox activity necessary for enhanced electronic conduction. Afterwards, the construct of fuel cell based on $Cu_{0.1}Sm_{0.1}CeO_2$ electrolyte exhibited the substantial and excellent performance reaching 902 mW cm^{-2} at 520 °C. Even though at lower operational temperature (470 °C), it maintains a relatively high-power output of 802 mW cm^{-2}. Upon reducing the temperature, it maintains its excellent electrochemical performance reaching power density of 565 and 363 mW cm^{-2} at 420 °C and 370 °C, respectively. This is due to delicately balancing ionic and electronic conduction, where the equimolar doping of Sm and Cu are crucial. The flexibility in exchange of copper's redox (Cu^{2+}/Cu^+) incorporate the controlled electronic characteristics, while Sm provides ample oxygen vacancies, which simultaneously support and improve the proton conduction. This synergistic balance is maintained down to 320 °C, where performance is recorded (190 mW cm^{-2}) as evident from figure 6(c). Hence, the intermediate doping levels (10% Cu and Sm) allow for optimized grain boundary conductivity, particularly at elevated temperatures, contributing to its superior overall performance. Moreover, $Cu_{0.15}Sm_{0.05}CeO_2$ electrolyte membrane-based fuel cell shows lower overall performance with peak power density of 718 mW cm^{-2} at 520 °C and rapidly dropped to just 119 mW cm^{-2} at 370 °C as shown in figure 6(d). The power density was not able be measured at 320 °C for $Cu_{0.15}Sm_{0.05}CeO_2$ electrolyte membrane-based fuel cell, the performance is not measurable. This can be attributed to the higher concentration of Cu than optimal ratio of Cu and also due to lower content of Sm, which resulted in a fewer oxygen vacancy. It is also possible that the higher copper concentration (15%) might introduce more electronic conduction pathways but also disrupt the grain boundary conduction due to the excessive formation of copper-rich phases. This imbalance between ionic and electronic conduction may explain the reduced fuel cell efficiency at lower temperatures.

Thus, we can extract several key factors which are responsible for the enhanced performance of $Cu_{0.1}Sm_{0.1}CeO_2$. Firstly, the careful co-doping of samarium and copper creates a synergistic effect that balances ionic and electronic conduction. As EIS analysis revealed, the grain boundary resistance is significantly lower than both bulk and electrode resistances between 520 °C and 420 °C, indicating effective ionic conduction through the grains. This behavior is essential in maintaining high conductivity consequently, high power density in the fuel cell. At temperatures below 420 °C, while the grain boundary resistance begins to exceed the bulk resistance, the carefully tailored microstructure still supports reasonable conductivity, preventing a drastic drop in performance. The morphological characterizations of $Cu_{0.1}Sm_{0.1}CeO_2$ further reinforce its superior electrochemical properties. The SEM images reveal spherically shaped particles, which promote favorable grain growth and minimize interfacial resistance between grains, supporting the EIS findings of lower grain boundary resistance. The cubic fluorite structure, as confirmed by F_{2g} Raman band analysis, suggests a stable oxygen vacancy environment, crucial for efficient ionic conduction. The presence of these oxygen vacancies, especially near grain boundaries, is central to the enhanced ionic transport that occurs in this material, particularly at higher operating temperatures. In terms of electronic conduction, $Cu_{0.1}Sm_{0.1}CeO_2$ shows a measured electronic conductivity of 0.019 S cm^{-1}, which strikes an optimal balance. This moderate level of electronic conductivity is high enough to contribute to the overall power density but not so high that it overwhelms the ionic contribution, which is crucial for effective electrolyte function in SOFCs. The DC polarization measurements underscore this balance, showing that with increased Cu-content, the electronic conduction steadily increases. However, it is $Cu_{0.1}Sm_{0.1}CeO_2$ that maintains the best compromise between the two conduction mechanisms. Excessive electronic conduction, as observed in $Cu_{0.15}Sm_{0.05}CeO_2$, leads to poorer overall fuel cell performance, highlighting the importance of this balance in achieving optimal results. Hence, the overall high performance of $Cu_{0.1}Sm_{0.1}CeO_2$ made it an ideal candidate as electrolyte for use in SOFC electrolytes. Its ability to maintain both ionic and electronic conduction, while minimizing power loss with demonstrates its robustness and efficiency in operating conditions typical of SOFC applications. The optimized $Cu_{0.1}Sm_{0.1}Ce_{0.8}O_2$ composition achieves superior performance with lower activation energy and higher power density than conventional electrolytes, emphasizing its promise for IT-SOFC applications as represented in table S1. This $Cu_{0.1}Sm_{0.1}CeO_2$ composition stands out among the tested materials as the most promising for high-performance fuel cells.

3.8. Verification of protonic conduction

Here we further compared the power outputs with and without a $BaZr_{0.9}Y_{0.1}O_3$ (BZY) buffer layer, the aim was to assess the protonic conductivity of the doped materials under realistic fuel cell conditions. The rationale behind testing is to explore how this proton-conducting layer affects the overall performance. The five-layer cell setup, incorporating a BZY layer positioned between the anode and cathode, is designed to block oxygen ions and electronic conduction, enabling only proton transport across the electrolyte [20]. Therefore, a comparison between the performance of the fuel cell based on pure $Cu_xSm_{0.2-x}Ce_{0.8}O_2$, $x = 0, 0.05, 0.10, 0.15$ compositions and

five-layer fuel cell provide key information on how much protonic conduction for each composition contributes to the fuel cell operation as illustrated in figures 6(e), (f) and supplementary data figure S7(a)–(b), while figure 6(g) presents the 3D visualization of power density performance for NCAL/BZY-CSC-BZY/NCAL and NCAL/CSC/NCAL configurations. For $Cu_{0.05}Sm_{0.15}CeO_2$, the power output at 520 °C with the BZY layer achieves a power density of 690 mW cm^{-2}. This corresponds to a power loss of approximately 18%, suggesting that the BZY layer slightly impedes electronic conduction but still allows reasonable ionic conductivity at high temperatures. But protonic conduction-based fuel cell using $Cu_{0.1}Sm_{0.1}CeO_2$ electrolyte, which shows the best performance among the compositions, the inclusion of the BZY layer leads to some power loss. The power output of the fuel cell based on $Cu_{0.1}Sm_{0.1}CeO_2$ electrolyte with BZY layers resulted 766 mW cm^{-2} at 520 °C, reflecting power losses of approximately 15% due to different factors specifically due to additional interfaces. This small drop indicates that the addition of the BZY layer has a minimal impact on $Cu_{0.1}Sm_{0.1}CeO_2$ composition proving that $Cu_{0.1}Sm_{0.1}CeO_2$ maintain more than 85% of proton conductivity. Subsequently, the power out of the fuel cell based on $Cu_{0.15}Sm_{0.05}CeO_2$ electrolyte with BZY layers, the performance drops with the power output of 606 mW cm^{-2} at 520 °C, resulting in 16% of the loss. Furthermore, figure S7(c)–(e) shows Nyquist plots of EIS that provide evidence for resistance values of Sm–Cu co-doped CeO$_2$ compositions. The general trend observed across all compositions is that the addition of the BZY layer provides better ionic conduction at high temperatures but introduces some resistance at lower temperatures, which restricts the overall power output. However, $Cu_{0.1}Sm_{0.1}CeO_2$ consistently outperforms better than other compositions in both scenarios. Furthermore, the incorporation of additional BZY layers did not cause any significant increase in Ohmic as well as grain boundary/interfacial resistances as can be observed in figure S7(c)–(e) and table S2. The slight rise in polarization resistance for all BZY-filtered Sm-Cu co-doped CeO$_2$ compositions due to the addition of extra layers is minimal and with the reported literature, not substantially affect the electrochemical performance of the fuel cell. This demonstrates that the extra layers did not hinder the proton transport, maintaining efficient charge transfer across the cell while contributing to overall stability without compromising the fuel cell's performance.

These entire performances can be further confirmed via ionic conductivity, therefore, the ionic conductivity with and without a BZY filter layer are shown in figures S8(a) and (b). Figure S8(c) depicts the Arrhenius plot with activation energies as a function of 1000 T^{-1} (K^{-1}) obtained from respective *I-V* and *I-P* curve of as-prepared SDC and Sm-Cu co-doped CeO$_2$ compositions, as a function of temperature. Figure S8(a) shows the ionic conductivity of the prepared compositions with BZY filter layers, where the five layers-based fuel cell resulted in protonic conductivity of entire compositions, reflecting a modest increase in the resistive barrier for ion transport due to a higher number of interfaces. However, $Cu_{0.1}Sm_{0.1}CeO_2$ continues to display substantial protonic conductivity (0.15 S cm^{-1}), confirming that it remains resilient

under the additional resistance imposed by the BZY layer. The slight increase in resistance due to the filter layer has not significantly impacted the overall conductivity, showing that these materials are well-suited for integration into multilayered SOFC architectures. In figure S8(b), the ionic conductivity of each composition is plotted as a function of 1000/T (K) in the temperature range of 520 °C-320 °C. Among these compositions, $Cu_{0.1}Sm_{0.1}CeO_2$ exhibits the highest ionic conductivity throughout the operational temperature. At 520 °C, a fuel cell based on $Cu_{0.1}Sm_{0.1}CeO_2$ electrolyte achieves ionic conductivity of 0.16 S cm^{-1} and reached the value of 0.055 S cm^{-1} at 320 °C. This indicates that the equimolar co-doping of Cu and Sm creates a more favorable environment for high ionic conductivity. As the temperature decreases, the conductivity drops for all samples, but interestingly $Cu_{0.1}Sm_{0.1}CeO_2$ maintains its ionic conductivity, demonstrating the benefits of an optimal balance between Cu^{2+} and Sm^{3+}. In contrast, $Sm_{0.2}Ce_{0.8}O_2$ shows the lowest conductivity (0.12 S cm^{-1}), suggesting that Sm doping alone is less effective for promoting oxygen vacancies and facilitating ion transport compared to Cu and Sm co-doping. In figure S8(c), the Arrhenius plot demonstrates the relationship between the ionic conductivity and temperature, with the calculated activation energies (E_a) derived from the slope of the plots. Among these, $Cu_{0.1}Sm_{0.1}CeO_2$ exhibits the lowest activation energy (0.31 eV), signifying the most efficient ionic conduction. The low activation energy is attributed to the optimal ratio of Cu^{2+} and Sm^{3+} co-doping, which facilitates enhanced oxygen vacancy generation and ion transport. $Cu_{0.5}Sm_{0.15}CeO_2$ and $Cu_{0.15}Sm_{0.05}CeO_2$ show slightly higher activation energies (0.43 eV and 0.45 eV, comparatively), indicating that variations in the ratio of Cu^{2+} and Sm^{3+} affect the ion migration energy barrier. In addition, $Sm_{0.2}Ce_{0.8}O_2$ has the highest activation energy (0.52 eV), demonstrating that Sm doping alone creates a higher energy barrier for ion conduction compared to co-doping with Cu^{2+}. Ionic conductivity and activation energy trends in Cu–Sm co-doped ceria (CSC) reveal 10% copper doping as the optimal concentration for achieving superior electrochemical performance as depicted in figure 6(h). These key scientific findings suggest that the co-doping strategy of Cu and Sm in ceria significantly lowers the activation energy for ionic conduction and enhances ionic conductivity. Furthermore, the study confirms dominant protonic conduction in prepared electrolyte materials as reported activation energies fall in the range of typical proton conductors [48, 49].

3.9. DRT analysis

In the analysis of DRT analysis experiment, a minimal hydrogen flow rate of 30 ml min^{-1} is utilized, which is adequate to sustain anodic activity and facilitate the HOR. DRT analysis, derived from EIS, is employed to precisely assess the cell kinetics and allows for the predominant observation of proton conductivity. The same experimental conditions and hydrogen/air flow rates are applied uniformly across all three tested compositions. After an initial air stabilization period, hydrogen is introduced and maintained for
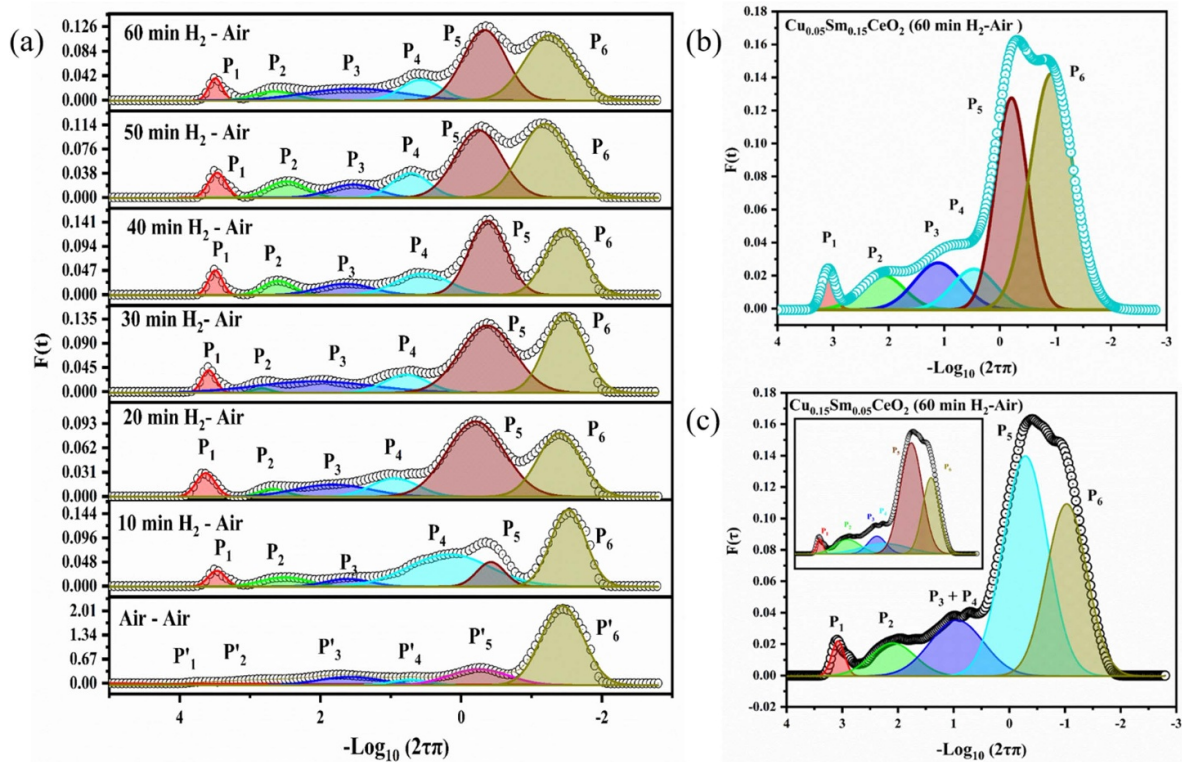
Figure 7. The DRT results for $Cu_{0.1}Sm_{0.1}Ce_{0.8}O_2$ cell at 520 °C representing sub-processes involved to demonstrate effect of electrochemical proton injection and grain boundary conduction from air/air to H_2/air atmosphere till 60 min (a), DRT results for $Cu_{0.05}Sm_{0.15}Ce_{0.8}O_2$ cell at 520 °C at 60 min of proton injection (b), DRT results for $Cu_{0.15}Sm_{0.05}Ce_{0.8}O_2$ cell at 520 °C at 60 min of proton injection (c).

60 min across all compositions. The DRT profiles depicted in figure 7(a) illustrate the progression of DRT for the cell composition NCAL/$Cu_{0.1}Sm_{0.1}Ce_{0.8}O_2$/NCAL in an air-to-hydrogen atmosphere transition, showing continuous proton injection. Figures 7(b) and 6(c) display the DRT spectra at 60 min for compositions $Cu_{0.05}Sm_{0.15}Ce_{0.8}O_2$ and $Cu_{0.15}Sm_{0.05}Ce_{0.8}O_2$, respectively, with supplementary figures S9(a) and (b) illustrating the temporal evolution of DRT for these cells. As figure 7(a) indicates, peak P_1' and P_2' correspond to the sub-process involving oxygen-ion transport and charge transfer within the electrodes, according to their frequency response [50]. Peaks P_3' to P_5' are linked to electrode processes such as oxygen reduction, incorporation into the lattice, and oxygen adsorption and dissociation [50–52]. Peak P_1 represents proton interfacial conduction and lattice incorporation, while peak P_2 is associated with proton formation (HOR) and hydrogen dissociation [53–55]. Peak P_3, appearing at intermediate frequencies, indicates oxygen incorporation into the lattice [50–52]. Peak P_4 is attributed to the ORR occurring on the air side, represented by the reaction $\left(2H^+ + \frac{1}{2}O_2 + 2e^- \leftrightarrow H_2O\right)$. Based on the spatial and temporal analysis of these peaks in both air/air and H_2/air configurations, peak P_5 belongs to the oxygen adsorption and dissociation, while the final peak P_6 is related to polarization effects due to gas diffusion [50–52]. The presence of peaks P_1, P_2, and P_3 suggests limited oxygen-ion conduction with dominant protonic conduction within the cell. The evidence is through peak area analysis as the corresponding peak area

decreases with the proton injection (from air atmosphere to proton injection). As P_1 decreases from 0.37 to a stable value of 0.01, P_2 decreases to a stable value of 0.014 from 0.248 and P_3 reduces to a stable value of 0.02 from 0.265 after just 40 min of proton injection. These peak area in DRT is related to the polarization resistance corresponding to the sub-process [53–55]. Similarly, P_4-P_6 has been reduced as well. A detailed comparison along with reduced area values is inserted in table S3. Reduced peak areas for P_4-P_6 means that the electrode reaction is accelerated after the proton injection. A comparison between the $Cu_{0.1}Sm_{0.1}Ce_{0.8}O_2$-electrolyte fuel cell and $Cu_{0.05}Sm_{0.15}Ce_{0.8}O_2$, $Cu_{0.15}Sm_{0.05}Ce_{0.8}O_2$ compositions-based fuel cells area and frequency shift calculation especially for P_1 can also give us some hints. It has been reported for proton transport on the surface of CeO_2 particles [56]. DRT results of $Cu_{0.05}Sm_{0.15}Ce_{0.8}O_2$ and $Cu_{0.15}Sm_{0.05}Ce_{0.8}O_2$ compositions are shown in figures 7(b), (c) and supplementary data figure S9(a)–(b). Comparing the frequency of P_1 for all three compositions after 60 min of proton injection, it is concluded that the frequency for P_1 is higher (44300) for $Cu_{0.10}Sm_{0.10}Ce_{0.8}O_2$ than $Cu_{0.05}Sm_{0.15}Ce_{0.8}O_2$ (15400 Hz) and $Cu_{0.15}Sm_{0.05}Ce_{0.8}O_2$ (15359 Hz) compositions. This means proton conduction in $Cu_{0.10}Sm_{0.10}Ce_{0.8}O_2$ is faster than in $Cu_{0.05}Sm_{0.15}Ce_{0.8}O_2$ and $Cu_{0.15}Sm_{0.05}Ce_{0.8}O_2$ compositions. A detailed comparison for frequency shift for all CSC compositions is inserted in tables S4 and S5.

Furthermore, the area of P_1 is smaller than P_3, which indicates that proton conduction and incorporation to lattice have
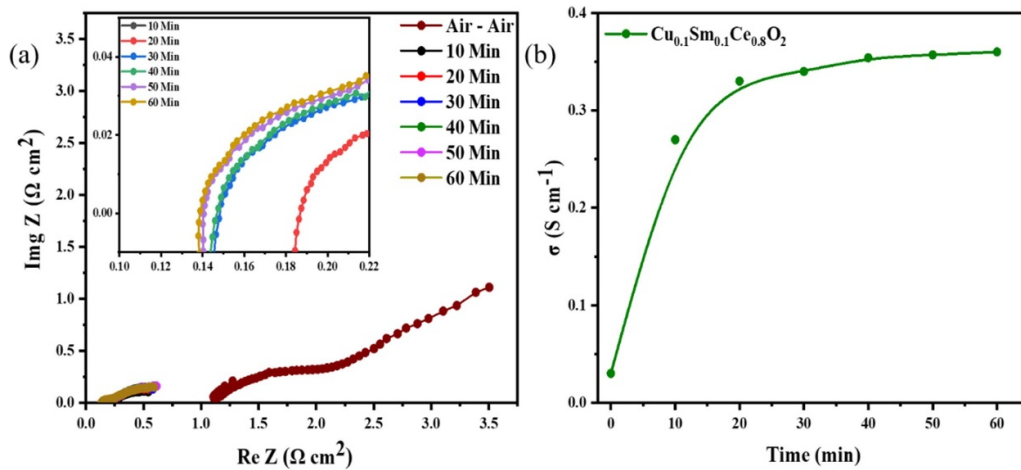
Figure 8. The Nyquist plot represents EIS data from air/air to H$_2$/air atmosphere for Cu$_{0.1}$Sm$_{0.1}$Ce$_{0.8}$O$_2$ (a), ionic conductivity plots of Cu$_{0.1}$Sm$_{0.1}$Ce$_{0.8}$O$_2$ as a function of time obtained from EIS (b).

less polarization resistance as compared to oxygen incorporation to lattice. More specifically, comparing the peaks P_4' and P_4 areas of ORR process, we can see that corresponding resistance under air is 0.10 Ω which rapidly decreases to 0.01 Ω within 20 min after proton injection during fuel cell process confirming accreted ORR after proton injection demonstrates that ORR process is shifted from
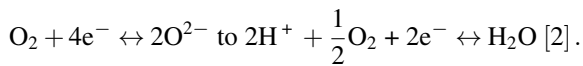
$$O_2 + 4e^- \leftrightarrow 2O^{2-} \text{ to } 2H^+ + \frac{1}{2}O_2 + 2e^- \leftrightarrow H_2O \text{ [2]}.$$

Figure 8(a) shows the change in EIS at different times for Cu$_{0.10}$Sm$_{0.10}$Ce$_{0.8}$O$_2$ composition. As shown in figure 8(b), the conductivity in the air atmosphere is 0.03 S cm^{-1}. As protons are injected, a rapid rise of conductivity is observed as calculated by EIS data figure 8(b) which increases ceaselessly up to 30 min and then achieves a stable plateau within 40 min. It is the result of the subsequent decrease in both grain boundary conduction resistance and polarization resistance, seen in the Nyquist plot, that supports this conclusion. Conductivity is increased faster in the first 30 min of injection by reaching the value of 0.30 S cm^{-1} and then changes slowly until the stabilizes at 3.5×10^{-1} S cm^{-1}.

Bode plot analysis is a key tool for understanding the frequency-dependent behavior of electrochemical systems, especially for SOFC electrolyte materials. It provides insights into how ionic and electronic conduction processes vary across low, medium, and high-frequency regions by examining the impedance magnitude and phase angle, which helps to interpret the underlying mechanisms of proton transport, interfacial polarization, and grain boundary effects [57, 58]. In figures 9(a)–(f), Bode plots for SDC and Cu$_{0.1}$Sm$_{0.1}$Ce$_{0.8}$O$_2$ at 520 °C (a)–(b), at 420 °C (c)–(d), and collective Bode plots at 520 °C and 420 °C (e)–(f) are shown, showcasing impedance magnitude (|Z|) and phase angle across low, medium, and high-frequency regions. Both SDC and Cu$_{0.1}$Sm$_{0.1}$Ce$_{0.8}$O$_2$ in the HF region exhibit a near-zero phase angle, as evident in figures 9(a) and (b). This behavior indicates the presence of purely resistive characteristics and the presence of bulk

ionic conduction, suggesting that the bulk material effectively conducts ions with minimal interfacial impedance [59, 60]. For Cu$_{0.1}$Sm$_{0.1}$Ce$_{0.8}$O$_2$, the presence of copper further facilitates proton transport within the material, evident from the lower impedance curve in the high-frequency region as compared to SDC. The MF region reveals different responses for SDC and Cu$_{0.1}$Sm$_{0.1}$Ce$_{0.8}$O$_2$. Here, Cu$_{0.1}$Sm$_{0.1}$Ce$_{0.8}$O$_2$ exhibits a lower phase angle than pure SDC, which corresponds to the presence of capacitive/inductive behavior due to grain boundary conduction [57, 58]. In proton-conducting electrolytes, grain boundaries can act as additional pathways for ion hopping, which is especially active in this frequency range [3]. The reduced impedance curve for Cu$_{0.1}$Sm$_{0.1}$Ce$_{0.8}$O$_2$ implies that Cu doping mitigates grain boundary resistance, possibly by generating active sites that ease proton transfer along grain boundaries [3, 57, 58]. This reduction in grain boundary resistance suggests that the Cu$_{0.1}$Sm$_{0.1}$Ce$_{0.8}$O$_2$ promotes effective proton conduction, enhancing the material's overall conductivity at mid-frequencies. In the LF region, Cu$_{0.1}$Sm$_{0.1}$Ce$_{0.8}$O$_2$ shows an initial phase angle drop followed by a return toward zero, a pattern absents in pure SDC (highlighted in figures 9(b)–(f)). The initial dip in phase angle points to a capacitive effect attributed to charge separation at the electrode/electrolyte interface, likely due to charge accumulation at the electrode/electrolyte interface, a phenomenon that Cu doping amplifies by enabling additional electronic pathways through Cu^{2+}/Cu$^+$ redox reactions. This enhances charge transfer across the electrode/electrolyte interface, promoting ORR and HOR kinetics at low operational temperatures [61]. The subsequent rise towards zero phase angle suggests a partial restoration of conductive pathways balancing ionic and electronic contributions within the material. At the lower temperature of 420 °C, both SDC and Cu$_{0.1}$Sm$_{0.1}$Ce$_{0.8}$O$_2$ compositions display phase angles approaching zero in the high and mid-frequency (HF and MF) ranges, (figures 9(c)–(f)) and then swiftly transition to slightly negative phase angles, highlighting the dominance of grain boundary conduction with minimal resistive losses, a finding confirmed by DRT experiment.
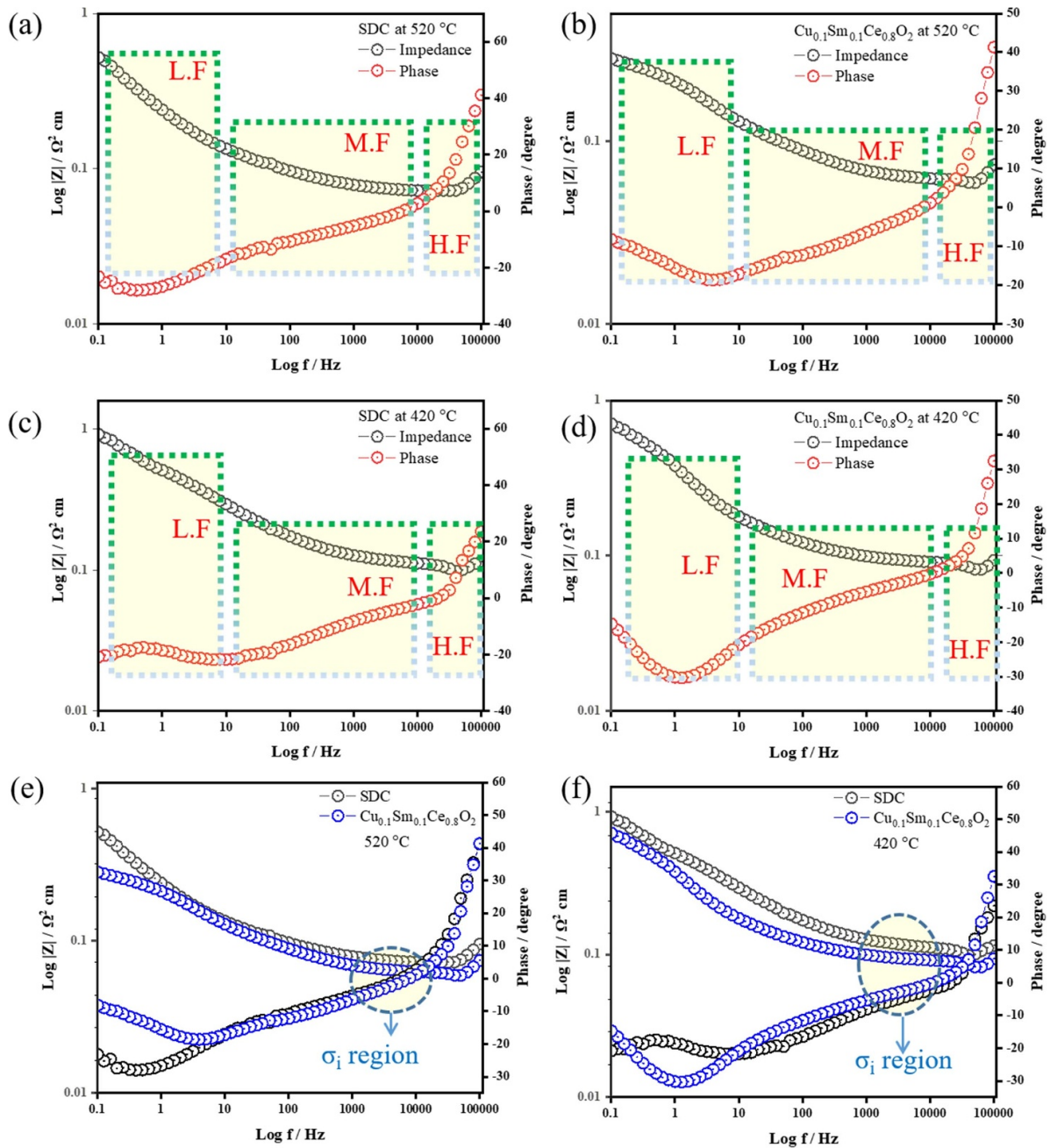
Figure 9. Bode plot showing impedance (|Z|) and phase angle across low-frequency (LF), medium-frequency (MF), and high-frequency (HF) regions for SDC and $Cu_{0.1}Sm_{0.1}Ce_{0.8}O_2$ 520 °C (a)–(b), at 420 °C (c)–(d), collective Bode plot analysis at 520 °C (e), collective Bode plot analysis at 320 °C (f).

Furthermore, in the MF range, Cu doping in SDC lowers the phase angle with a reduced impedance curve (figures 9(c)–(f)), indicating reduced grain boundary resistance. This optimizes ionic conduction across grain boundaries, which enhances electrolyte performance and stability, particularly under low-temperature SOFC conditions. In essence, Cu doping strengthens bulk conduction in the HF region, enhances grain boundary conduction in the MF region, and introduces beneficial capacitive effects in the LF region, all of which contribute to improved electrochemical performance in SOFCs.

3.10. Stability test with post stability structural characterizations

The long-term stability of the 10-CSC electrolyte was systematically evaluated under fuel cell operating conditions at a constant current density of 110 mA cm^{-2} and a temperature of 520 °C, with H$_2$ as the fuel and air as the oxidant. As depicted in figure 10(a), the cell voltage exhibited negligible degradation over a period of 320 h of continuous operation, reflecting the substantial operational stability of the 10-CSC electrolyte. Initially, there was a short activation period during which the
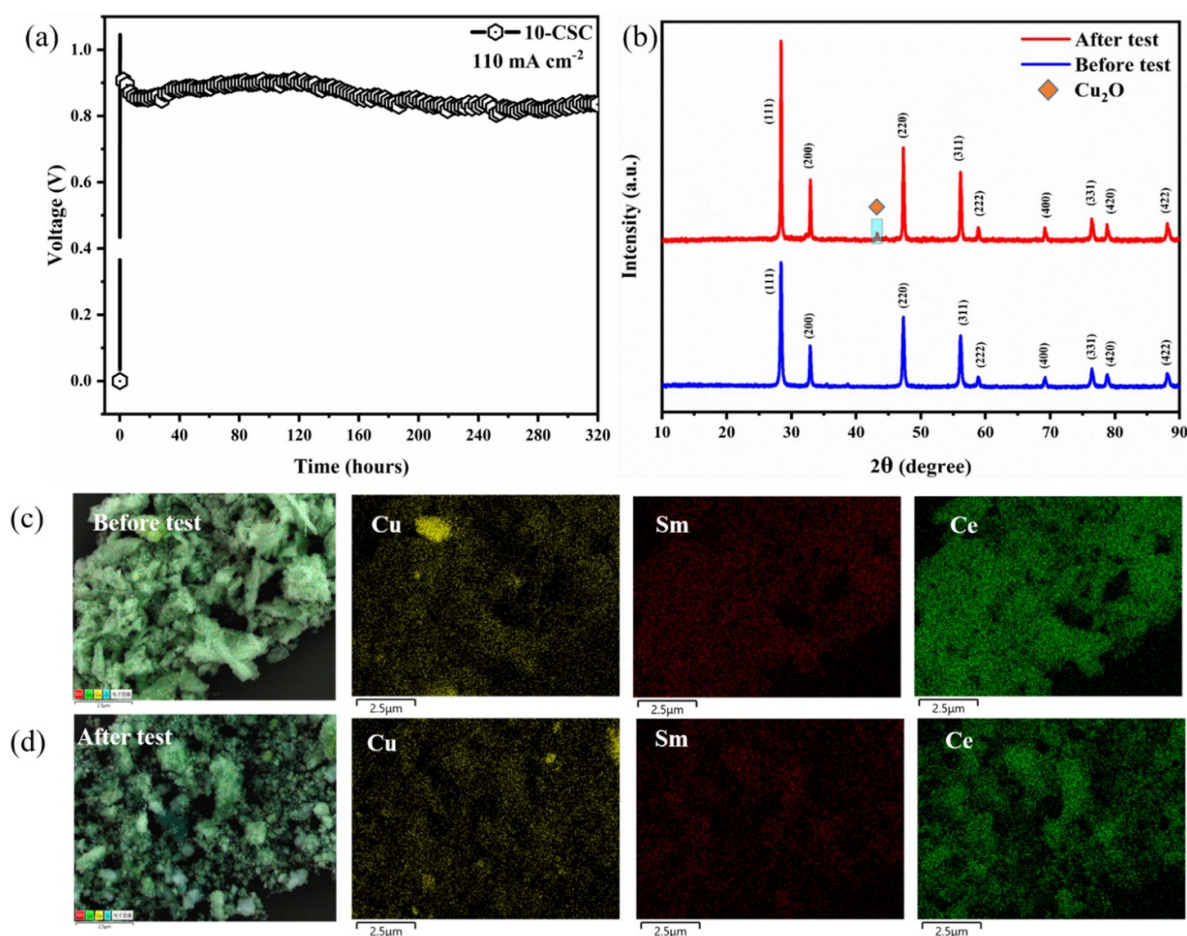
Figure 10. Stability performance of the Cu-Sm co-doped ceria electrolyte under H_2/air operation at a constant current density of 110 mA cm^{-2} and 520 °C for 320 h (a), x-ray diffraction (XRD) patterns before and after the test, showed no significant phase changes apart from minor peak corresponding to Cu_2O, confirming structural stability (b), EDX mapping images of 10-CSC before (c), and after (d) stability testing including cerium (Ce), copper (Cu), and samarium (Sm).

voltage increased, followed by a steady stabilization phase, where the cell maintained a consistent voltage output. This stable performance signifies the material's remarkable resistance to redox cycling, indicating that the electrolyte can withstand the oxidative and reducing environments typical in fuel cell operation. Additionally, the electrolyte in the cell showed minimal signs of interfacial degradation, supporting the structural integrity of the designed 10-CSC electrolyte. These findings suggest that the co-doping strategy not only stabilizes the material during prolonged operation but also enhances its ability to maintain high ionic conductivity and electrochemical activity over time. Post-stability characterization, including XRD and EDS analysis, provided further evidence of the electrolyte's robust performance. These techniques confirmed the absence of phase degradation and no leaching out of any doped element, underscoring the durability and resilience of the 10-CSC electrolyte-based cell under long-term fuel cell conditions.

Following the stability test, XRD analysis and EDS mapping realized the post-structural and elemental composition characterizations. The XRD data (figure 10(b)) revealed broadening of the peaks and the appearance of a new peak

associated with Cu_2O after the stability test due to the reversible oxidation-reduction cycling that occurs during operation [61]. XRD results showed that the electrolyte materials of Cu and Sm co-doping into Ceria in cell demonstrated stable operation, where the overall cubic fluorite structure remained intact, moreover, the XRD patterns depicted that Cu(II) remains the predominant form of copper in 10-CSC after the stability test. These findings provide robust evidence that 10-CSC exhibits outstanding long-term stability under fuel cell operating conditions, maintaining both structural integrity and chemical stability over extended periods. Furthermore, figure 10(c) depicted the EDS mapping of cerium (Ce), copper (Cu), and samarium (Sm) before and after the stability test, where it can be seen that each element is homogenously distributed with similar intensities. It can be seen that XRD pattern and EDS mapping before and after the stability test revealed unaltered phase of 10-CSC materials and a uniform distribution of copper and samarium within the cerium matrix, indicating that copper and samarium are well-integrated into the lattice structure. The samarium (Sm) is also homogeneously dispersed, suggesting a stable initial state of the 10-CSC. After the stability test, shown in figure 10(d), the distribution of cerium

and samarium remains consistent with no noticeable segregation or phase changes. Copper continues to be evenly distributed, with no evidence of copper migration or aggregation. Importantly, the XRD analysis showed no significant phase degradation, confirming that these operational conditions did not compromise the material's chemical integrity or ionic conductivity. Instead, they demonstrate the material's resilience and ability to maintain stable performance under extended fuel cell conditions.

3.11. Proposed mechanism of proton conduction

In the Sm-Cu co-doped CeO_2 system, the transport mechanism is driven by proton conduction mainly, supported by the formation of oxygen vacancies and the interaction between the dopant cations and the ceria lattice [62]. Both samarium (Sm^{3+}) and copper (Cu^{2+}/Cu^{+}) play critical roles in enhancing proton mobility, while the material's microstructure and morphological characteristics strongly influence overall performance. The microstructure of the Sm–Cu co-doped CeO_2 materials plays a pivotal role in facilitating protonic conduction, particularly at the grain boundaries. The material is synthesized at a relatively low sintering temperature of 750 °C, which leads to smaller grain sizes and a higher density of grain boundaries [63, 64]. These grain boundaries serve as primary pathways for proton conduction, where oxygen vacancies are more mobile compared to the bulk of the material. This observation is consistent with the EIS analysis, where grain boundary resistance is lower than bulk resistance. The grain boundaries effectively provide short diffusion paths for protons, allowing for enhanced ionic transport [3, 57, 58].

This dual doping strategy results in a high concentration of oxygen vacancies, creating multiple pathways for proton conduction. Protons (H^{+}) from adsorbed water vapor or hydrogen gas occupy these vacancies, allowing efficient transport across the lattice via a hopping mechanism [65]. Protons hop between adjacent oxygen ions via these vacancies, facilitating ionic conduction, which is particularly dominant at the grain boundaries due to the higher vacancy concentration in these regions [66]. The redox flexibility of copper (Cu^{2+}/Cu^{+}) introduces additional functionality to the material, contributing to both ionic and electronic conduction. The redox couple Cu^{2+}/Cu^{+} provides an electron reservoir that supports electron transfer alongside proton transport, a phenomenon known as E-I coupling. E-I coupling in Cu-Sm co-doped ceria is enhanced by Cu^{2+}/Cu^{+} redox cycling and oxygen vacancy formation, facilitating localized electronic transfer and ionic conductivity. This synergistic mechanism, supported by XPS, EDX, and XRD results, ensures optimized performance and stability under operational conditions.

The adjacent oxidation states of Ce (Ce^{4+}/Ce^{3+}), Cu (Cu^{2+}/Cu^{+}) and Sm^{3+} enable dynamic redox reactions, which facilitate charge compensation and stabilize oxygen vacancies, further enhancing proton conduction [3, 37–40]. This E-I coupling mechanism adds a layer of versatility to the material, as the introduction of electronic conduction does not hinder proton transport but rather complements it at intermediate to high temperatures. The co-doped material effectively balances ionic and electronic conductivity, which is crucial for applications such as SOFCs, where mixed conduction can improve overall device efficiency.

3.12. Future perspectives on mechanical properties and chemical compatibility

Building on the comprehensive electrochemical and post-stability analyses presented in this work, future investigations into the mechanical properties and chemical compatibility of Cu-Sm co-doped CeO_2 are recommended to further substantiate its practical applicability in SOFCs. While this study has thoroughly addressed ionic conductivity, structural stability, and long-term performance, evaluating the material's mechanical resilience, including resistance to thermal stress, fracture toughness, and durability during prolonged operation, is critical for its large-scale application. Furthermore, chemical compatibility studies are essential to assess potential interactions between Cu-Sm co-doped CeO_2 and electrode materials under high-temperature conditions. Understanding interfacial stability, reaction kinetics, and diffusion processes at the electrode-electrolyte interface will ensure optimal integration into SOFC systems.

These additional investigations, coupled with the extensive results presented here, will provide a holistic understanding of Cu-Sm co-doped CeO_2 as a robust and reliable electrolyte material for next-generation SOFC technologies.

4. Conclusion

This study marks a breakthrough in IT-SOFC electrolyte development, demonstrating that co-doping Sm^{3+} and Cu^{2+} into ceria dramatically enhances electrochemical performance. The $Cu_{0.1}Sm_{0.1}CeO_2$ composition, with its unique balance of oxygen vacancy-driven proton conduction and Cu^{2+}-enabled electronic transport, achieved outstanding results across structural and electrochemical analyses. DRT and EIS data confirmed a significant reduction in grain boundary resistance, enabling superior proton conductivity at intermediate temperatures, while validating the efficacy of Cu^{2+} redox coupling. The designed $Cu_{0.1}Sm_{0.1}Ce_{0.8}O_{2-\delta}$ material as acted electrolyte-based fuel cell generated peak power density of 902 mW cm^{-2} at 520 °C underscores its potential for high-performance fuel cells, offering both stability and minimal resistance. Importantly, the addition of a BZY filter layer introduced only a marginal increase in resistance, underscoring the stability and robustness of this material. The Bode plot findings for Cu-Sm-CeO_2 highlight its enhanced grain boundary conduction, stable bulk conduction, and improved interfacial charge dynamics, making it an effective electrolyte material for low-temperature SOFCs. This work showcases the power of strategic co-doping in tailoring material properties and sets a new benchmark for IT-SOFC electrolyte technologies, paving the way for future innovations in fuel cell performance and durability.

5. Future perspectives

The development of semiconductor ionic membranes (SIMs) represents a promising pathway to overcoming key limitations in current fuel cell technologies. SIMs uniquely combine both ionic and electronic conductive properties, enabling their use in low-temperature SOFCs (LT-SOFCs) with enhanced electrochemical performances [67]. The ability to optimize both ionic and electronic transport/transfer through surface and interface engineering is a key advantage, potentially improving the efficiency of IT-SOFCs while reducing operational costs by lowering temperature requirements [68]. Advancements in doping strategies, particularly through multi-dopant systems, can further optimize defect chemistry and enhance ionic-electronic coupling, offering improved conductivity [3, 69]. Recently, even di-electric materials are tuned to perform under fuel cell conditions [70]. These developments are crucial for scaling SIM-based electrolytes for commercial LT-SOFC applications, where cost-effective and scalable production methods, such as solution-based co-precipitation and advanced sintering, will be essential. Beyond SOFCs, SIMs show considerable promise for use in hydrogen production, carbon capture, and energy storage, where their mixed conduction properties can be leveraged for multifunctional applications [3]. Machine learning and computational modeling are expected to play an increasing role in accelerating the discovery of novel SIM compositions, optimizing dopant levels, and simulating electrochemical performance, which will expedite the development of next-generation materials [71, 72]. Finally, to ensure long-term operational stability, SIMs will require enhanced grain boundary engineering and protective coatings to mitigate degradation under harsh fuel cell conditions. These advances will be critical for realizing the full potential of SIMs as reliable, high-performance electrolytes in next-generation fuel cell technologies [73].

Data availability statement

The data can be provided upon request.

Authors contributions

S. R., and B. Z.,: Conceptualization, Methodology, S. S., Z.T., A. M.,: Software, Data curation, S. S., and S. R: Writing—original draft, S. R., and M. T.,: Support material Characterizations, S. R., A. M., M. T., A.N.A., and MAK Yousaf Shah: Visualization, Investigation, Software, Validation. S. S., S. R., and B. Z: Writing—review & editing. S. R., B.Z.,: Secure funding projects. S.R., and B. Z.,: Designed the research topic and overall supervisions.

Conflict of interest

The authors declare that they have no known competing financial interests or personal relationships that could have appeared to influence the work reported in this paper.

ORCID iD

Sajid Rauf ⬤ https://orcid.org/0000-0003-2343-9334

References

[1] Lu Y, Mi Y, Li J, Qi F, Yan S and Dong W 2021 Recent progress in semiconductor-ionic conductor nanomaterial as a membrane for low-temperature solid oxide fuel cells *Nanomaterials* **11** 2290

[2] Zhu B, Mi Y, Xia C, Wang B, Kim J-S, Lund P and Li T 2021 A nanoscale perspective on solid oxide and semiconductor membrane fuel cells: materials and technology *Energy Mater.* **1** 100002

[3] Tayyab Z *et al* 2024 Theoretical and experimental explored tailored hybrid H^+/O^{2-} ions conduction: Bridged for high performance fuel cell and water electrolysis *Chem. Eng. J.* **482** 148750

[4] Lu Y, Zhu B, Shi J and Yun S 2021 Advanced low-temperature solid oxide fuel cells based on a built-in electric field *Energy Mater.* **1** 100007

[5] Abdulwahab K O, Khan M M and Jennings J 2023 Doped ceria nanomaterials: preparation, properties, and uses *ACS Omega* **8** 30802–23

[6] Koettgen J, Grieshammer S, Hein P, Grope B O, Nakayama M and Martin M 2018 Understanding the ionic conductivity maximum in doped ceria: trapping and blocking *Phys. Chem. Chem. Phys.* **20** 14291–321

[7] Zha S, Xia C and Meng G 2003 Effect of Gd (Sm) doping on properties of ceria electrolyte for solid oxide fuel cells *J. Power Sources* **115** 44–48

[8] Fu Y P, Wen S B and Lu C 2008 Preparation and characterization of samaria-doped ceria electrolyte materials for solid oxide fuel cells *J. Am. Ceram. Soc.* **91** 127–31

[9] Acharya S, Gaikwad V, D'Souza S and Barman S 2014 Gd/Sm dopant-modified oxidation state and defect generation in nano-ceria *Solid State Ion.* **260** 21–29

[10] Dholabhai P P, Adams J B, Crozier P and Sharma R 2010 A density functional study of defect migration in gadolinium doped ceria *Phys. Chem. Chem. Phys.* **12** 7904–10

[11] AlKhoori A A, Polychronopoulou K, Belabbes A, Abi Jaoude M, Vega L F, Sebastian V, Hinder S, Baker M A and Zedan A F 2020 Cu, Sm co-doping effect on the CO oxidation activity of CeO_2. A combined experimental and density functional study *Appl. Surf. Sci.* **521** 146305

[12] Konsolakis M and Ioakeimidis Z 2014 Surface/structure functionalization of copper-based catalysts by metal-support and/or metal–metal interactions *Appl. Surf. Sci.* **320** 244–55

[13] Zhang J, Tse K, Wong M, Zhang Y and JJFop Z 2016 A brief review of co-doping *Front. Phys.* **11** 1–21

[14] Chien A C, Ye N J, Huang C-W and Tseng I-H 2021 Studies of nickel/samarium-doped ceria for catalytic partial oxidation of methane and effect of oxygen vacancy *Catalysts* **11** 731

[15] Montini T, Melchionna M, Monai M and Fornasiero P 2016 Fundamentals and catalytic applications of CeO_2-based materials *Chem. Rev.* **116** 5987–6041

[16] Namkhai P and Jang K 2022 Co-doping effect on the optical properties of $Eu^{(2+/3+)}$ doped in $BaSiO_3$ *Materials* **15** 6559

[17] Ganesh K S, Wang B, Kim J-S and Zhu B 2019 Ionic conducting properties and fuel cell performance developed by band structures *J. Phys. Chem.* C **123** 8569–77

[18] Dong Y, Hampshire S, Zhou J, Dong X, Lin B and Meng G 2011 Combustion synthesis and characterization of Cu–Sm co-doped CeO_2 electrolytes *J. Eur. Ceram. Soc.* **31** 2365–76

[19] Zhu B *et al* 2015 Schottky junction effect on high performance fuel cells based on nanocomposite materials *Adv. Energy Mater.* **5** 1401895

[20] He Z, Nie J, Liu K, Ganesh K S, Akbar M, Xia C, Wang X, Dong W, Huang J and Wang B 2021 Compositing protonic conductor $BaZr_{0.5}Y_{0.5}O_3$ (BZY) with triple conductor $BaCo_{0.4}Fe_{0.4}Zr_{0.1}Y_{0.1}O_{3-\delta}$ (BCFZY) as electrolyte for advanced solid oxide fuel cell *Int. J. Hydrog. Energy* **46** 9799–808

[21] Xia C, Mi Y, Wang B, Lin B, Chen G and Zhu B 2019 Shaping triple-conducting semiconductor $BaCo_{0.4}Fe_{0.4}Zr_{0.1}Y_{0.1}O_{3-\delta}$ into an electrolyte for low-temperature solid oxide fuel cells *Nat. Commun.* **10** 1707

[22] Rauf S *et al* 2024 Highly active interfacial sites in SFT-SnO_2 heterojunction electrolyte for enhanced fuel cell performance via engineered energy bands: envisioned theoretically and experimentally *Energy Environ. Mater.* **7** e12606

[23] Shah M Y, Lu Y, Mushtaq N, Alomar M, Yousaf M, Akbar N, Arshad N, Irshad M S and Zhu B 2024 Uncovering proton transportation enabled via the surface and interfacial engineering for ceramic fuel cells *Int. J. Hydrog. Energy* **55** 491–501

[24] Kuntaiah K, Sudarsanam P, Reddy B M and Vinu A 2013 Nanocrystalline Ce_{1-x} Sm_x $O_{2-\delta}$ (x = 0.4) solid solutions: structural characterization versus CO oxidation *RSC Adv.* **3** 7953–62

[25] Kurajica S, Ivković I K, Dražić G, Shvalya V, Duplančić M, Matijašić G, Cvelbar U and Mužina K 2022 Phase composition, morphology, properties and improved catalytic activity of hydrothermally-derived manganese-doped ceria nanoparticles *Nanotechnology* **33** 135709

[26] Hernández W, Laguna O, Centeno M and Odriozola J 2011 Structural and catalytic properties of lanthanide (La, Eu, Gd) doped ceria *J. Solid State Chem.* **184** 3014–20

[27] Dubey K, Dubey S, Sahu V, Modi A, Bamne J, Haque F Z and Gaur N K 2023 Defects and oxygen vacancies modified properties of transition metal doped $Ce_{0.95}X_{0.05}O_2$ (X = Fe, Co, Ni) nanoparticles *Mater. Sci. Eng.* B **288** 116154

[28] Xu S, Sun D, Liu H, Wang X and Yan X 2011 Fabrication of Cu-doped cerium oxide nanofibers via electrospinning for preferential CO oxidation *Catal. Commun.* **12** 514–8

[29] Andrade J D 1985 X-ray photoelectron spectroscopy (XPS) *Surface and Interfacial Aspects of Biomedical Polymers* vol 1 ed K L Mittal (Plenum Press New York) pp 105–95

[30] Kim N-Y, Kim G, Sun H, Hwang U, Kim J, Kwak D, Park I-K, Kim T, Suhr J and Nam J-D 2022 A nanoclustered ceria abrasives with low crystallinity and high Ce^{3+}/Ce^{4+} ratio for scratch reduction and high oxide removal rates in the chemical mechanical planarization *J. Mater. Sci.* **57** 12318–28

[31] Soni S, Vats V, Kumar S, Dalela B, Mishra M, Meena R, Gupta G, Alvi P A and Dalela S 2018 Structural, optical and magnetic properties of Fe-doped CeO_2 samples probed using x-ray photoelectron spectroscopy *Mater. Electron.* **29** 10141–53

[32] Paparazzo E 2011 On the curve-fitting of XPS Ce (3d) spectra of cerium oxides *Mater. Res. Bull.* **46** 323–6

[33] Paunović N, Dohčević-Mitrović Z, Scurtu R, Aškrabić S, Prekajski M, Matović B and Popović Z V 2012 Suppression of inherent ferromagnetism in Pr-doped CeO_2 nanocrystals *Nanoscale* **4** 5469–76

[34] Yashima M, Sasaki S, Yamaguchi Y, Kakihana M, Yoshimura M and TJApl M 1998 Internal distortion in ZrO_2–CeO_2 solid solutions: neutron and high-resolution synchrotron x-ray diffraction study *Appl. Phys. Lett.* **72** 182–4

[35] Kahsay A W, Ibrahim K B, Tsai M-C, Birhanu M K, Chala S A, Su W-N and Hwang B-J 2019 Selective and low overpotential electrochemical CO_2 reduction to formate on CuS decorated CuO heterostructure *Catal. Lett.* **149** 860–9

[36] Svintsitskiy D A, Kardash T Y, Stonkus O A, Slavinskaya E M, Stadnichenko A I, Koscheev S V, Chupakhin A P and Boronin A I 2013 *In situ* XRD, XPS, TEM, and TPR study of highly active in CO oxidation CuO nanopowders *J. Phys. Chem.* C **117** 14588–99

[37] Fan L, Zhu B, Su P-C and He C 2018 Nanomaterials and technologies for low temperature solid oxide fuel cells: recent advances, challenges and opportunities *Nano Energy* **45** 148–76

[38] Artini C, Carnasciali M, Viviani M, Presto S, Plaisier J, Costa G and Pani M 2018 Structural properties of Sm-doped ceria electrolytes at the fuel cell operating temperatures *Solid State Ion.* **315** 85–91

[39] Kuharuangrong S J 2007 Ionic conductivity of Sm, Gd, Dy and Er-doped ceria *J. Power Sources* **171** 506–10

[40] Beckers J and Rothenberg G 2008 Redox properties of doped and supported copper–ceria catalysts *Dalton Trans.* **46** 6573–8

[41] Waldow S P, Wardenga H, Beschnitt S, Klein A and De Souza R A 2019 Concentration and diffusivity of oxygen interstitials in niobia-doped ceria *J. Phys. Chem.* C **123** 6340–50

[42] Soni S, Kumar S, Dalela B, Kumar S, Alvi P and Dalela S 2018 Defects and oxygen vacancies tailored structural and optical properties in CeO_2 nanoparticles doped with Sm_{3+} cation *J. Alloys Compd.* **752** 520–31

[43] Mushtaq N, Xia C, Dong W, Wang B, Raza R, Ali A, Afzal M and Zhu B 2019 Tuning the energy band structure at interfaces of the $SrFe_{0.75}Ti_{0.25}O_{3-\delta}$–$Sm_{0.25}Ce_{0.75}O_{2-\delta}$ heterostructure for fast ionic transport *ACS Appl. Mater. Interfaces* **11** 38737–45

[44] Jung G-B, Huang T-J and Chang C-L 2002 Effect of temperature and dopant concentration on the conductivity of samaria-doped ceria electrolyte *J. Solid State Electrochem.* **6** 225–30

[45] Yu Y, Shah M Y, Wang H, Cheng X, Guo L, Huang J, Lund P and Zhu B 2024 Synergistic proton and oxygen ion transport in fluorite oxide-ion conductor *Energy Mater. Adv.* **5** 0081

[46] Lin Y, Fang S, Su D, Brinkman K S and Chen F 2015 Enhancing grain boundary ionic conductivity in mixed ionic–electronic conductors *Nat. Commun.* **6** 6824

[47] Wang K, Cui Y, Ni J and Ni C 2024 Cu doping enhanced the performance of $BaFe_{0.8}Zr_{0.1}Y_{0.1}O_{3-\delta}$ cathode for a proton-conducting solid oxide fuel cell at low temperature *Int. J. Hydrog. Energy* **57** 1316–24

[48] Ye W, Hu Q, Zhao H, Jing Y, Singh M and Fan L 2024 *In situ* reconstruction of proton conductive electrolyte from self-assembled perovskite oxide-based nanocomposite for low temperature ceramic fuel cells *Chem. Eng. J.* **497** 154977

[49] Duan C, Huang J, Sullivan N and O'Hayre R 2020 Proton-conducting oxides for energy conversion and storage *Appl. Phys. Rev.* **7** 011314

[50] Li M, Ren Y, Zhu Z, Zhu S, Chen F, Zhang Y and Xia C 2016 La$_{0.4}$Bi$_{0.4}$Sr$_{0.2}$FeO$_{3-\delta}$ as cobalt-free cathode for intermediate-temperature solid oxide fuel cell *Electrochim. Acta* **191** 651–60

[51] Wang J, Li Z, Zang H, Sun Y, Zhao Y, Wang Z, Zhu Z, Wei Z and Zheng Q 2022 BaZr$_{0.1}$Fe$_{0.9-x}$Ni$_x$O$_{3-\delta}$ cubic perovskite oxides for protonic ceramic fuel cell cathodes *Int. J. Hydrog. Energy* **47** 9395–407

[52] Shi N, Su F, Huan D, Xie Y, Lin J, Tan W, Peng R, Xia C, Chen C and Lu Y 2017 Performance and DRT analysis of P-SOFCs fabricated using new phase inversion combined tape casting technology *J. Mater. Chem.* A **5** 19664–71

[53] Guo R and He T 2022 High-entropy perovskite electrolyte for protonic ceramic fuel cells operating below 600 C *ACS Mater. Lett.* **4** 1646–52

[54] Guo R, Li D, Guan R, Kong D, Cui Z, Zhou Z and He T 2022 Sn–Dy–Cu Triply Doped BaZr$_{0.1}$Ce$_{0.7}$Y$_{0.2}$O$_{3-\delta}$: a chemically stable and highly proton-conductive electrolyte for low-temperature solid oxide fuel cells *ACS Sustain. Chem. Eng.* **10** 5352–62

[55] Yu S, Wang Z, Yang L, Liu J, Guan R, Xiao Y and He T 2021 Enhancing the sinterability and electrical properties of BaZr$_{0.1}$Ce$_{0.7}$Y$_{0.2}$O$_{3-\delta}$ proton-conducting ceramic electrolyte *J. Am. Ceram. Soc.* **104** 329–42

[56] Xing Y, Wu Y, Li L, Shi Q, Shi J, Yun S, Akbar M, Wang B, Kim J-S and Zhu B 2019 Proton shuttles in CeO$_2$/CeO$_{2-\delta}$ core–shell structure *ACS Energy Lett.* **4** 2601–7

[57] Goswami N and Kant R 2019 Theory for impedance response of grain and grain boundary in solid state electrolyte *J. Electroanal. Chem.* **835** 227–38

[58] Laschuk N O, Easton E B and Zenkina O V 2021 Reducing the resistance for the use of electrochemical impedance spectroscopy analysis in materials chemistry *RSC Adv.* **11** 27925–36

[59] Matos B J 2020 The genuine ac-to-dc proton conductivity crossover of nafion and polymer dielectric relaxations as a fuel cell polarization loss *J. Electroanal. Chem.* **871** 114357

[60] Ail U, Phopase J, Nilsson J, Khan Z U, Inganäs O, Berggren M and Crispin X 2020 Effect of sulfonation level on lignin/carbon composite electrodes for large-scale organic batteries *ACS Sustain. Chem. Eng.* **8** 17933–44

[61] Zhang G, Liu X, Wang L, Xing G, Tian C and Fu H 2022 Copper collector generated Cu$^+$/Cu^{2+} redox pair for enhanced efficiency and lifetime of Zn–Ni/Air hybrid battery *ACS Nano* **16** 17139–48

[62] Nolan M J 2011 Enhanced oxygen vacancy formation in ceria (111) and (110) surfaces doped with divalent cations *J. Mater. Chem.* **21** 9160–8

[63] Grieshammer S 2021 The effect of defect interactions on the reduction of doped ceria *Phys. Chem. Chem. Phys.* **23** 10321–5

[64] Andersson D A, Simak S I, Skorodumova N V, Abrikosov I A and Johansson B 2006 Optimization of ionic conductivity in doped ceria *Proc. Natl Acad. Sci.* **103** 3518–21

[65] Sun X, Vøllestad E, Rørvik P M, Prodinger S, Kalantzopoulos G N, Chatzitakis A and Norby T 2023 Surface protonic conductivity in chemisorbed water in porous nanoscopic CeO$_2$ *Appl. Surf. Sci.* **611** 155590

[66] Wang B, Zhu B, Yun S, Zhang W, Xia C, Afzal M, Cai Y, Liu Y, Wang Y and Wang H 2019 Fast ionic conduction in semiconductor CeO$_{2-\delta}$ electrolyte fuel cells *npg Asia Mater.* **11** 51

[67] Bibi B *et al* 2025 Emerging semiconductor ionic materials tailored by mixed ionic-electronic conductors for advanced fuel cells *Adv. Powder Mater.* **3** 100231

[68] Zhu B *et al* 2021 Semiconductor electrochemistry for clean energy conversion and storage *Electrochem. Energy Rev.* **4** 757–92

[69] Sharif M S *et al* 2024 Semiconductor ionic Cu doped CeO$_2$ membrane fuel cells *Ceram. Int.* **50** 40350–62

[70] Rauf S *et al* 2025 Alternative strategy for development of dielectric calcium copper titanate-based electrolytes for low-temperature solid oxide fuel cells *Nano-Micro Lett.* **17** 1–23

[71] Zuccarini C, Ramachandran K and Jayaseelan D D 2024 Material discovery and modeling acceleration via machine learning *APL Mater.* **12** 090601

[72] Correa-Baena J-P, Hippalgaonkar K, van Duren J, Jaffer S, Chandrasekhar V R, Stevanovic V, Wadia C, Guha S and Buonassisi T 2018 Accelerating materials development via automation, machine learning, and high-performance computing *Joule* **2** 1410–20

[73] Singh M, Paydar S, Singh A K, Singhal R, Singh A and Singh M 2024 Recent advancement of solid oxide fuel cells towards semiconductor membrane fuel cells *Energy Mater.* **4** 400012